Monthly Notices of the ROYAL ASTRONOMICAL SOCIETY

MNRAS **444,** 268–289 (2014) doi:10.1093/mnras/stu1395

Mass and magnification maps for the *Hubble Space Telescope* Frontier Fields clusters: implications for high-redshift studies

Johan Richard,[1⋆] Mathilde Jauzac,[2,3] Marceau Limousin,[4] Eric Jullo,[4] Benjamin Clément,[5] Harald Ebeling,[6] Jean-Paul Kneib,[7] Hakim Atek,[7] Priya Natarajan,[8] Eiichi Egami,[5] Rachael Livermore[9] and Richard Bower[3]

[1]*CRAL, Observatoire de Lyon, Université Lyon 1, 9 Avenue Ch. André, F-69561 Saint Genis Laval Cedex, France*
[2]*Astrophysics and Cosmology Research Unit, School of Mathematical Sciences, University of KwaZulu-Natal, Durban 4041, South Africa*
[3]*Institute for Computational Cosmology, Durham University, South Road, Durham DH1 3LE, UK*
[4]*Laboratoire d'Astrophysique de Marseille, CNRS- Université Aix-Marseille, 38 rue F. Joliot-Curie, 13388 Marseille Cedex 13, France*
[5]*Steward Observatory, University of Arizona, 933 N. Cherry Avenue, Tucson, AZ 85721, USA*
[6]*Institute for Astronomy, University of Hawaii, 2680 Woodlawn Drive, Honolulu, HI 96822, USA*
[7]*Laboratoire d'Astrophysique, Ecole Polytechnique Fédérale de Lausanne, Observatoire de Sauverny, CH-1290 Versoix, Switzerland*
[8]*Department of Astronomy, Yale University, 260 Whitney Avenue, New Haven, CT 06511, USA*
[9]*Department of Astronomy, the University of Texas at Austin, 2515 Speedway Stop C1400, Austin, TX 78712, USA*

Accepted 2014 July 7. Received 2014 June 25; in original form 2014 May 11

ABSTRACT

Extending over three *Hubble Space Telescope* (*HST*) cycles, the Hubble Frontier Fields (HFF) initiative constitutes the largest commitment ever of *HST* time to the exploration of the distant Universe via gravitational lensing by massive galaxy clusters. Here, we present models of the mass distribution in the six HFF cluster lenses, derived from a joint strong- and weak-lensing analysis anchored by a total of 88 multiple-image systems identified in existing *HST* data. The resulting maps of the projected mass distribution and of the gravitational magnification effectively calibrate the HFF clusters as gravitational telescopes. Allowing the computation of search areas in the source plane, these maps are provided to the community to facilitate the exploitation of forthcoming HFF data for quantitative studies of the gravitationally lensed population of background galaxies. Our models of the gravitational magnification afforded by the HFF clusters allow us to quantify the lensing-induced boost in sensitivity over blank-field observations and predict that galaxies at $z > 10$ and as faint as m(AB) = 32 will be detectable, up to 2 mag fainter than the limit of the *Hubble Ultra Deep Field*.

Key words: galaxies clusters: individual: Abell 370 – galaxies clusters: individual: A1063S – galaxies clusters: individual: Abell 2744 – galaxies clusters: individual: MACS J0416.1−2403 – galaxies clusters: individual: MACS J0717.5+3745 – galaxies clusters: individual: MACS J1149.5+2223.

1 GRAVITATIONAL LENSING

At the end of the 1980s, the discovery of giant luminous arcs in clusters of galaxies (e.g. Soucail et al. 1988) and the realization that they can be explained by gravitational lensing (the bending of light by massive foreground mass concentrations) opened a new and powerful route to studying the distant Universe. Gravitational lensing can be understood as a geometrical mapping of the source plane on to the image plane, a mapping that depends on the surface mass distribution in the deflector and on the angular-diameter distances between the observer and the source, and the lens and the source, respectively (see the review by Kneib & Natarajan 2011). For extreme mass concentrations, the mapping is non-linear, producing magnified and highly distorted multiple images of a single background source. Such multiple images have been successfully exploited since the early 1990s (e.g. Kneib et al. 1996) to constrain the detailed mass distribution in cluster cores as well as to probe the mass distributions of samples of X-ray-selected clusters out to the virial radius (e.g. Smith et al. 2005; Ebeling et al. 2009; Richard et al. 2010b; Zitrin et al. 2012). Importantly, lensing also enables the study of distant background galaxies that would be unobservable without the magnification provided by the cluster lens (e.g. Ellis et al. 2001; Kneib et al. 2004; Richard et al. 2008;

⋆E-mail: johan.richard@univ-lyon1.fr

Bouwens et al. 2009; Coe et al. 2013), and offers the tantalizing possibility of measuring the geometry of the Universe through the accurate determination of cosmological distances (Soucail, Kneib & Golse 2004; Jullo et al. 2010).

The power of clusters as well-calibrated telescopes for studies of the distant Universe has become fully appreciated only in recent years. Highly active areas of research aiming to unveil the characteristics of individual galaxies at $1 < z < 5$ (e.g. Smail et al. 2007; Swinbank et al. 2009; Richard et al. 2011; Livermore et al. 2012) or to constrain statistically the properties of the galaxy population at $z > 5$ (e.g. Bouwens et al. 2011) all benefit greatly from gravitational amplification of the respective background sources. State-of-the-art lens-modelling techniques that combine strong-lensing constraints from large numbers of multiple-image systems with high-quality weak-lensing data can measure the mass in cluster cores (and thus the gravitational amplification along a given line of sight) to an accuracy of a few per cent (e.g. Bradač et al. 2006, 2009; Jullo et al. 2007; Jullo & Kneib 2009).

The necessary robust and efficient identification of multiple-image systems requires both high angular resolution and colour information. The unparalleled power of *Hubble Space Telescope* (*HST*) for such studies is exemplified by the identification of 42 multiple-image systems in Advanced Camera for Surveys (ACS) observations of the massive cluster Abell 1689 (Broadhurst et al. 2005), 24 of them with measured redshifts from deep Keck and VLT spectroscopy (Limousin et al. 2007). The ability to obtain spectra for gravitationally amplified galaxies at high redshift is a critical advantage over similar work conducted on non-magnified galaxies in the field, and crucial for the exploration of the end of the Dark Ages, one of the most ambitious and timely quests of present-day astrophysics. Although impressive progress has been made in this research area with the help of moderately deep observations of cluster lenses (e.g. Postman et al. 2012), a dedicated in-depth observational effort is needed if the scientific promise and potential of gravitational lensing by clusters is to be fully exploited.

This important next step forward is now being taken in the form of the Hubble Frontier Fields (HFF), a recent initiative launched by the Space Telescope Science Institute. As part of the preparations for these unprecedented observations of lensing clusters, five independent teams have analysed the existing imaging and spectroscopic data to provide the community with accurate mass models on each cluster. We describe in this paper the work performed by one of these groups, the CATS (Clusters As TelescopeS) team.

2 THE HFF

The *HST* Frontier Fields initiative, announced in the spring of 2013, devotes 140 orbits of *HST* time to deep imaging observations of each of six carefully selected cluster lenses. As a compromise between depth and spectral coverage, each target field will be observed for 20 orbits in each of the *F*435*W*, *F*606*W*, and *F*814*W* filters (all ACS), as well as in the *F*105*W*, *F*125*W*, *F*140*W*, and *F*160*W* filters (all WFC3), reaching $m \approx 29$ (AB) uniformly in all passbands. The total commitment of 840 orbits of Director's Discretionary Time is spread out over three cycles, starting with Cycle 21, with two clusters being targeted per cycle.

The HFF clusters were selected by an expert team recruited from the extragalactic community, trying to balance scheduling and follow-up constraints with the primary goal of the project: to identify clusters of maximal lensing strength (high gravitational magnification over a large angular area) whose angular size is well matched to the ACS field of view. The resulting list of HFF clusters comprises, in order of observation

Name	z	Reference
Abell 2744	0.308	Abell (1958)
MACS J0416.1−2403	0.396	Mann & Ebeling (2012)
MACS J0717.5+3745	0.545	Ebeling et al. (2007)
MACS J1149.5+2223	0.544	Ebeling et al. (2007)
Abell S1063	0.348	Abell, Corwin & Olowin (1989)
Abell 370	0.375	Abell (1958)

More information on the HFF initiative, both scientific and technical, can be found on the *HST* Frontier Fields homepage.[1]

All six HFF clusters have previously been targeted with *HST*. These observations were instrumental in the selection of the respective clusters for the HFF project as highly efficient gravitational lenses. Unlike A370, the first cluster lens to be discovered (Soucail et al. 1988; Richard et al. 2010a), most of the remaining HFF targets are much more recent discoveries made by the Massive Cluster Survey (MACS, Ebeling, Edge & Henry 2001). As a result, many of the existing *HST* observations of these fields were obtained only in the past few years and could thus take advantage of *HST*'s current state-of-the-art instruments. Further details are provided in Table A1 which lists all imaging observations performed with broad-band filters on ACS and WFC3.

Fig. 1 shows the outlines of the area targeted by the planned HFF observations overlaid on the existing *HST* imaging data. Note that, in all cases, the blank flanking fields fall outside the area covered by the existing data; hence, the gravitational magnification induced at the location of the flanking fields by either the clusters themselves, or by large-scale structure in their immediate vicinity, can presently not be constrained with *HST* data.

3 STRONG-LENSING FEATURES

3.1 Identifications

We now review, for each cluster, the associations of multiple images found in these *HST* images prior to HFF observations and used to constrain the strong-lensing models (see Section 4). We adopt the term 'system' for a set of multiple images arising from the same source, and the notation XY to describe image Y of system X (see Tables 1–6 and Figs 1–8 for each cluster in turn). We build our identification of multiple systems from earlier published lists of multiple images (identified either by our own or by other groups). For clusters having such a large number of constraints, our parametric analysis is quite sensitive to wrong identifications: we therefore added iteratively new systems and used the current model to predict additional counter-images. In a few cases, where the identification was ambiguous between multiple candidates, these counter-images were not added as constraints.

3.1.1 Abell 2744

An earlier strong-lensing analysis of this cluster was previously published by Merten et al. (2011), who identified 11 systems and

[1] http://www.stsci.edu/hst/campaigns/frontier-fields/

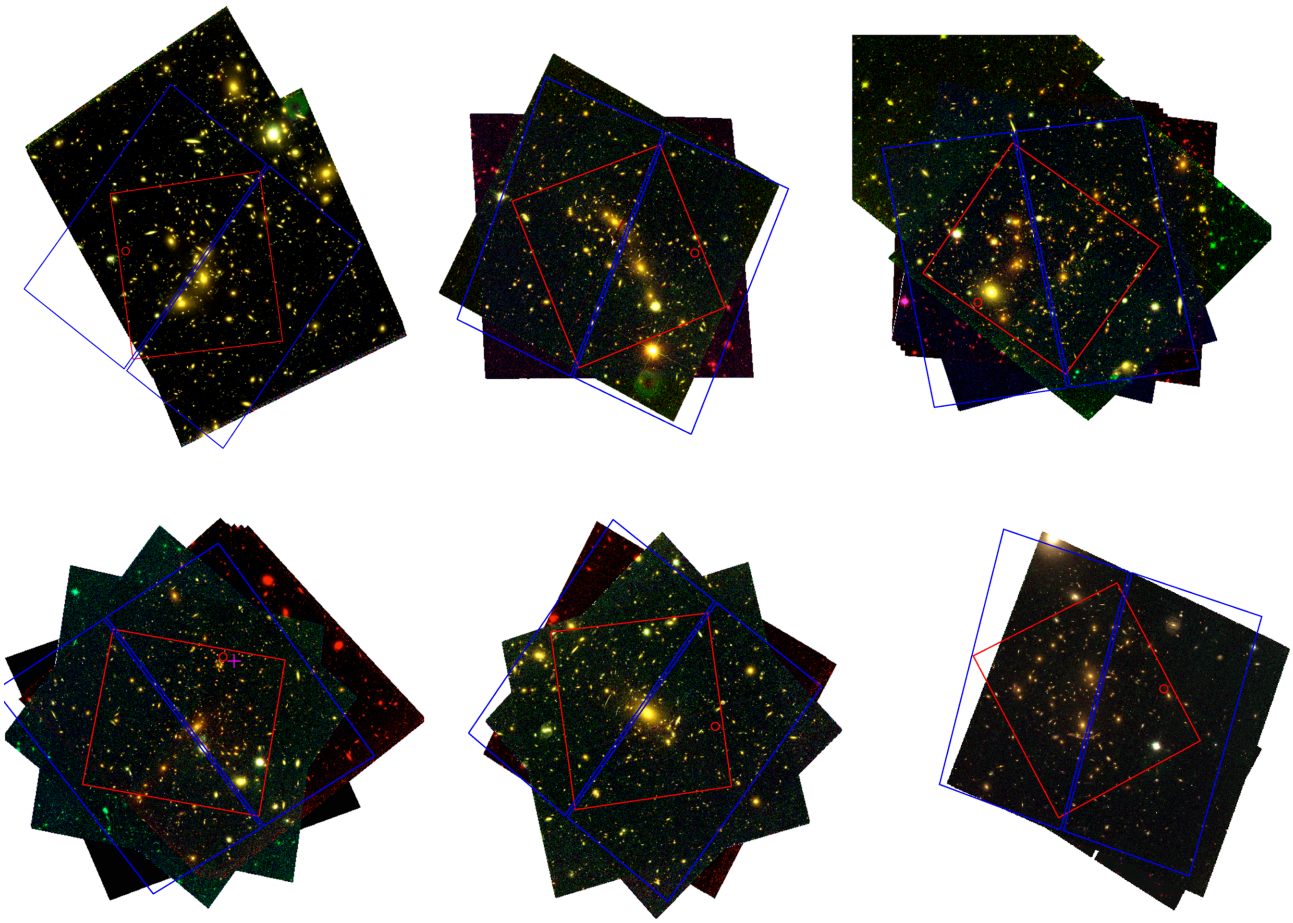

Figure 1. Colour images (*F*435*W*+*F*606*W*+*F*814*W*) of the archival *HST* data for the HFF (except for A370 where we show *F*475*W*+*F*625*W*+*F*814*W*). Overlaid in blue (red) are the apertures of the planned, deep HFF observations with ACS (WFC3). In all cases, the parallel flanking fields – which fall well outside the depicted area – have not been previously imaged with *HST*. The images shown are trimmed to the regions in which data in at least two filters are available whose central wavelengths differ by at least 150 Å, thus providing colour information suitable for the identification of multiple-image systems.

a total of 34 images. We build from these 11 systems and identify seven additional, convincing systems of multiple images (Fig. 3), leading to a total of 55 images. The majority of these new systems are located around the core of the cluster, but three new systems are identified around several sub-clumps (galaxy-scale) groups close to the north and north-west limits of the ACS coverage (Fig. 2). These sub-clumps were identified as 'N' and 'NW', respectively, in Merten et al. (2011).

Compared to Merten et al. (2011), we removed image 8.3 from our list of constraints, as its colours and location do not match well for a multiple system (in particular, the geometry should be similar to system 3). In addition, we do not find any convincing counter-image (third image of a triple 'fold' configuration) for systems 14, 15, and 18.

3.1.2 *MACS J0416*

Zitrin et al. (2013) presented a strong-lensing model with 23 systems identified in this cluster in the new CLASH (Postman et al. 2012) data, producing in total 70 images. Due to the very elongated nature of the cluster mass distribution (Fig. 4), all systems appear as triply imaged configurations. Among the total list of 23 systems, 10 systems and 36 images were considered by Zitrin et al. (2013) as less robust candidate multiple images.

We have built from this list of strong-lensing features and selected only the most robust systems and a few candidate systems showing clear counter-images based on our preliminary strong-lensing analysis (Table 2). New spectroscopic information (see Section 3.2.2) was also incorporated to help with this selection. In total, our final list contains 17 systems and 47 images. We do not identify a reliable (unambiguous) third image for systems 5, 8, 9, and 12.

3.1.3 *MACS J0717*

The set of multiply imaged systems used in the analysis of MACS J0717 mainly follows the one described in Limousin et al. (2012), with a few exceptions that we discuss here. The location of image 1.5 has been revisited, following Medezinski et al. (2014). System 2 has been removed from the analysis, after discussion between the different teams, given its faintness.

In addition, we added new spectroscopic redshifts measurements, in agreement with our previous estimates, obtained by the GLASS survey (Schmidt et al. 2014) for three multiple systems (4, 6, and 12).

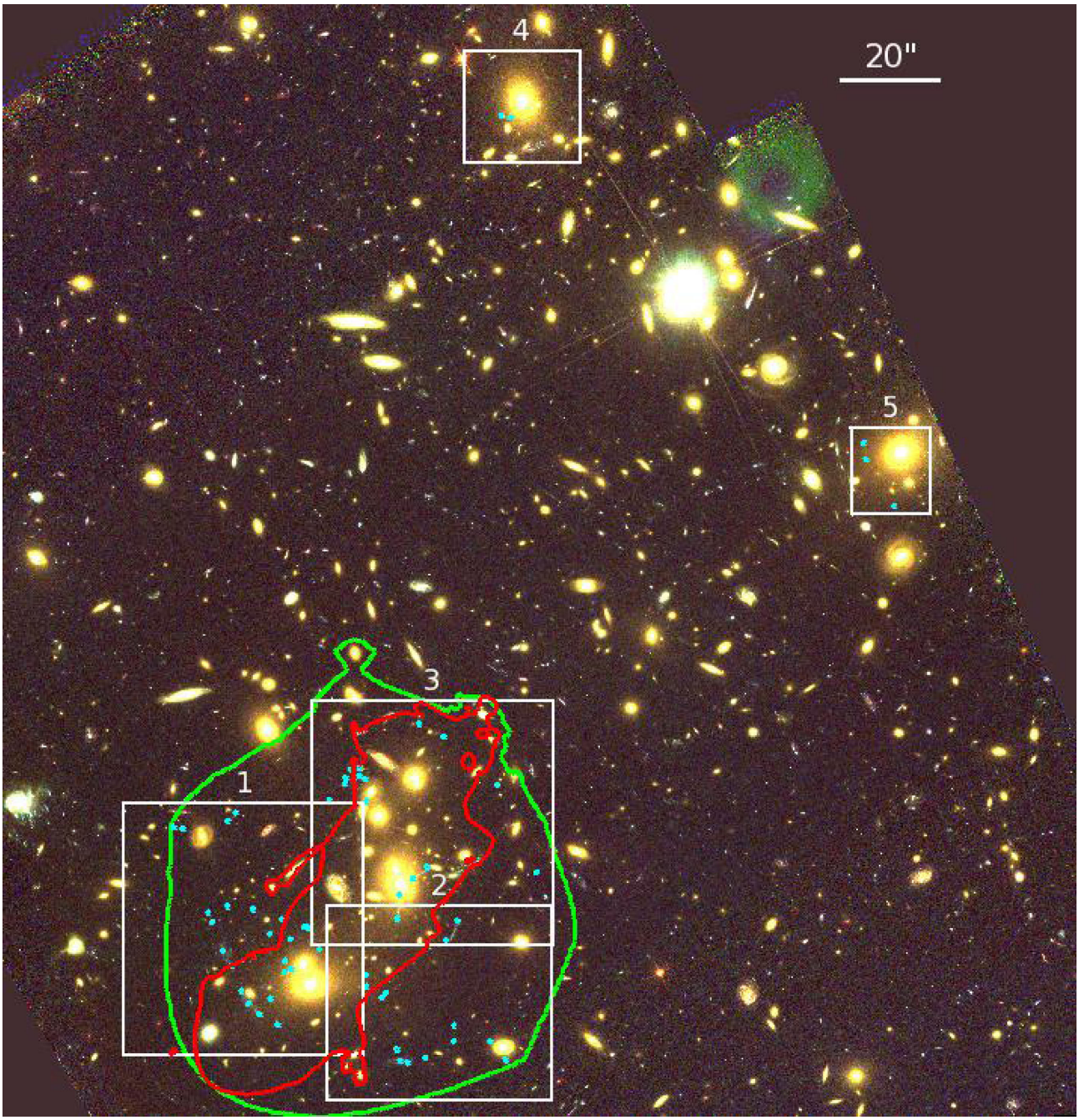

Figure 2. Colour image of A2744 as obtained with *HST*/ACS (*F*435*W*+*F*606*W*+*F*814*W*). North is up and east is left. Shown in red is the critical line at $z = 7$, in green the enclosing region where we expect multiple images at $z = 7$, and blue circles mark the location of multiple images used as constraints in the modelling. Thin white lines delineate the regions shown in more detail in Fig. 3.

Finally, Vanzella et al. (2014) recently measured a spectroscopic redshift $z = 6.4$ for two galaxies which we confirm to be multiply imaged with three images identified based on the mass model. We add this new constraint as system 19.

3.1.4 MACS J1149

The set of multiply imaged systems used in the analysis of MACS J1149 is based on the one presented by Smith et al. (2009), with the addition of six new systems as proposed by Zitrin et al. (2011): systems 5, 6, 7, 8, 13, and 14.

3.1.5 Abell S1063

We identify in this cluster 14 multiply imaged systems, all in a configuration of three images except for system 6 which shows as a quad (Boone et al. 2013). The robustness of these systems has been checked with a dedicated spectroscopic follow-up (Section 3.2.5). While this paper was being written, Monna et al. (2014) presented their own identifications, partially overlapping with our own list: we identify four additional systems and they identified two additional candidate systems which appear much fainter and less robust. In total, our list comprises 41 images of the 14 systems, as we do not find an unambiguous counterpart for systems 10 and 12.

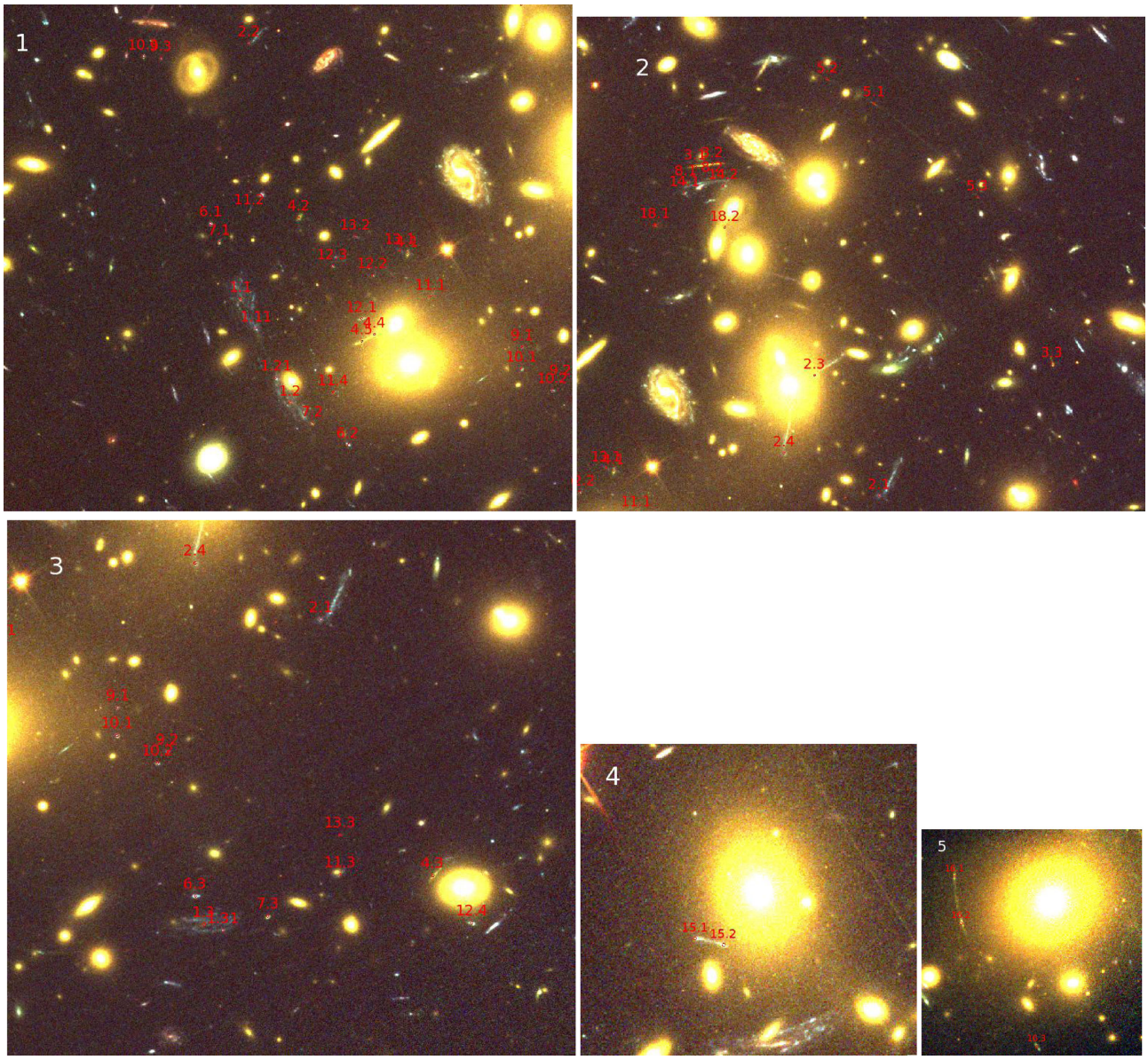

Figure 3. Sub-regions of A2744 as marked and labelled in Fig. 2. Strong-lensing features as listed in Table 1 are labelled.

3.1.6 Abell 370

Our strong-lensing analysis builds from the work published in Richard et al. (2010a), where we identified nine multiply imaged systems (as well as a faint radial arc, system 10). New *HST*/WFC3 images have been taken since this publication and allowed us to identify two additional systems. In total, we use 11 systems producing 34 images (Table 6).

3.2 Spectroscopy of strong-lensing features

Whenever possible, we use spectroscopic redshifts of multiply imaged systems to constrain the lens model. This information is important since the source redshifts are degenerate with the absolute values of the model parameters characterizing the mass distribution. All our models are anchored by spectroscopic redshifts for two to eight different multiple-image systems. We use spectroscopic redshifts from the literature, results shared among the different HFF mass modelling groups, and values obtained by us as part of dedicated spectroscopic follow-up observations. In the latter case, we provide below the details of the observations, data reduction, and analysis of these spectra.

3.2.1 A2744

We targeted the core of this cluster as part of our VLT/FOcal Reducer and low dispersion Spectrograph (FORS2) spectroscopic follow-up of submillimeter sources from the Herschel Lensing Survey (Egami et al. 2010). 10 multiple-image systems were observed in Multi-Object Spectroscopy (MOS) mode for a total of 2 h exposure time during the night of 2011 September 3 (ESO programme 087.B-0560(A), PI: Richard). We used a slit width of 1 arcsec, the GRIS_300V grism and the *GG*345 filter to cover the wavelength

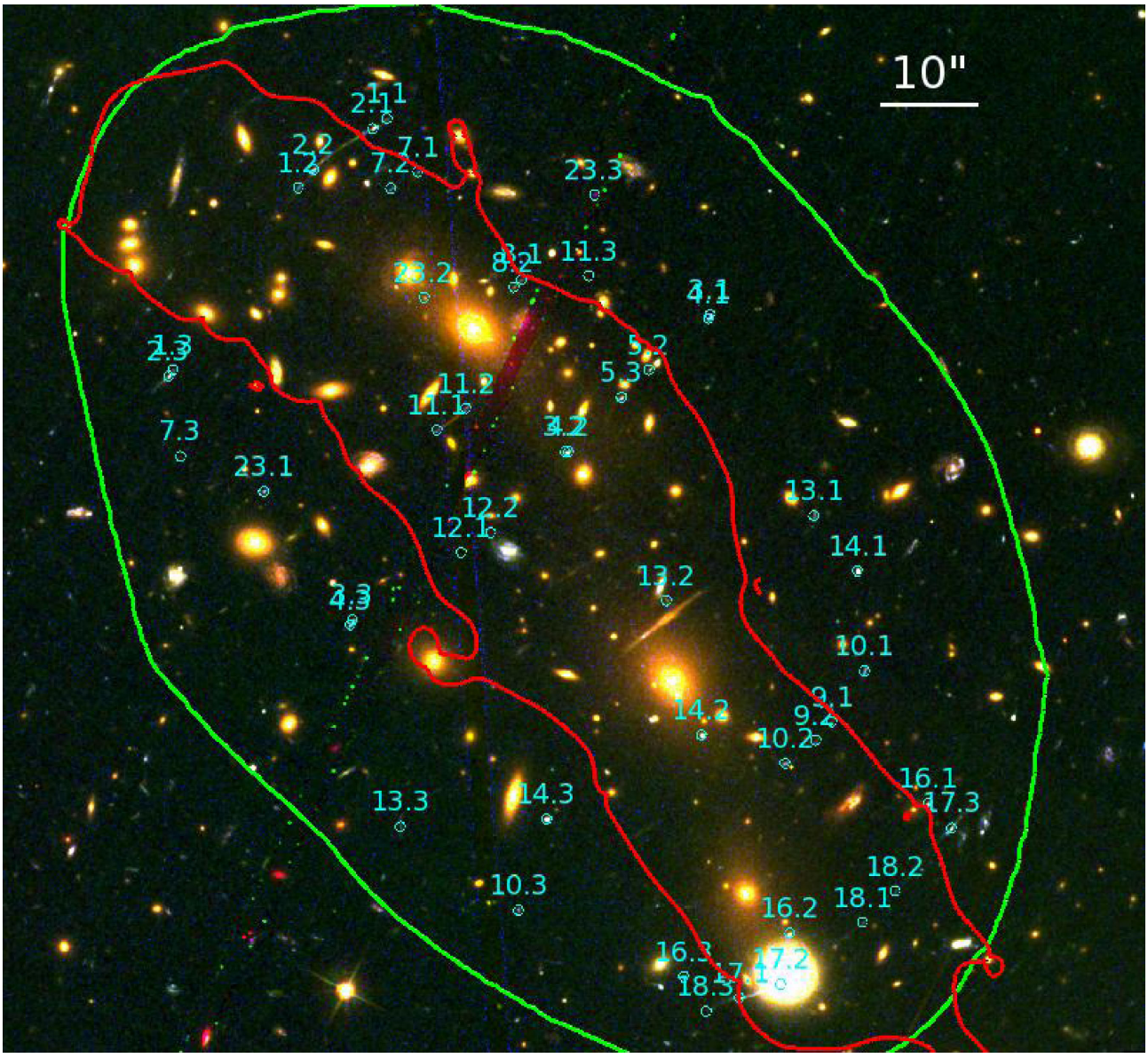

Figure 4. Same as Fig. 2 but for MACS J0416 and filter combination *F*435*W*+*F*606*W*+*F*814*W*.

range from 4300 to 9200 Å, albeit at low resolution ($R \sim 500$–1000) and a dispersion of 2 Å pixel^{-1}.

Of the strongly lensed sources targeted, redshifts could be secured for image A2744-4.3 at $z = 3.58$, through strong Lyman α emission (Fig. 9), in agreement with the photometric redshift of $z = 3.5 \pm 0.3$ reported by Merten et al. (2011). The spectrum of object 6.1 was found to feature a single narrow emission line at 5760 Å on top of a very blue continuum. The absence of other emission lines in the wavelength range covered agrees with C III] at $z = 2.019$, which is compatible with our prediction based on a preliminary lens model.

3.2.2 *MACS J0416*

We use spectroscopic redshifts for seven systems in MACS J0416.1−2403 (systems 2, 3, 7, 10, 13, 14, and 17) obtained as part of VLT programme 186.A-0798 (Balestra et al., in preparation; Grillo et al. 2014), and shared among the different HFF mass modelling groups. We also include spectroscopic redshifts for system 1, published by our group in Christensen et al. (2012).

3.2.3 *MACS J0717*

Since the analysis by Limousin et al. (2012), which presents our earlier observations on arc spectroscopy, one new spectroscopic redshift $z = 6.4$ has been measured for system 19, as described previously. We use spectroscopic redshifts for six systems in total (systems 1, 3, 13, 14, 15, and 19), ranging from $z = 1.850$ to 6.4.

3.2.4 *MACS J1149*

Since the analysis by Smith et al. (2009), no new spectroscopic redshifts have been measured in MACS J1149. We use spectroscopic redshifts for three systems (systems 1 to 3) at $z = 1.490$, 1.894, and 2.497. We refer to Smith et al. (2009) for details regarding arc spectroscopy.

Table 1. Strong-lensing features identified in the existing *HST* images of A 2744. Spectroscopic redshifts are listed under $z_{\rm prior}$ where available; other constraints used during the optimization process are quoted as a range, enclosed in square brackets.

ID	α (deg)	δ (deg)	$z_{\rm prior}$	$z_{\rm model}$
1.1	00:14:23.41	−30:24:14.10	[0.6–6.0]	1.72 ± 0.07
1.2	00:14:23.03	−30:24:24.56		
1.3	00:14:20.69	−30:24:35.95		
2.1	00:14:19.98	−30:24:12.06	[0.6–6.0]	2.33 ± 0.12
2.2	00:14:23.35	−30:23:48.21		
2.3	00:14:20.50	−30:23:59.63		
2.4	00:14:20.74	−30:24:07.66		
3.1	00:14:21.45	−30:23:37.95	[0.6–6.0]	2.34 ± 0.13
3.2	00:14:21.31	−30:23:37.69		
3.3	00:14:18.60	−30:23:58.44		
4.1	00:14:22.11	−30:24:09.48	3.58	
4.2	00:14:22.95	−30:24:05.84	3.58	
4.3	00:14:19.30	−30:24:32.13	3.58	
4.4	00:14:22.37	−30:24:17.69	3.58	
4.5	00:14:22.46	−30:24:18.38	3.58	
5.1	00:14:20.02	−30:23:31.45	[0.6–6.0]	3.50 ± 0.47
5.2	00:14:20.40	−30:23:28.95		
5.3	00:14:19.19	−30:23:41.14		
6.1	00:14:23.65	−30:24:06.48	2.019	
6.2	00:14:22.57	−30:24:28.84	2.019	
6.3	00:14:20.74	−30:24:33.74	2.019	
7.1	00:14:23.58	−30:24:08.35	[0.6–6.0]	2.63 ± 0.17
7.2	00:14:22.85	−30:24:26.73		
7.3	00:14:20.30	−30:24:35.33		
8.1	00:14:21.53	−30:23:39.62	[0.6–6.0]	5.12 ± 0.79
8.2	00:14:21.32	−30:23:39.20		
9.1	00:14:21.21	−30:24:18.98	[0.6–6.0]	4.60 ± 0.35
9.2	00:14:20.91	−30:24:22.47		
9.3	00:14:24.04	−30:23:49.75		
10.1	00:14:21.22	−30:24:21.16	[0.6–6.0]	6.00 ± 0.25
10.2	00:14:20.97	−30:24:23.33		
10.3	00:14:24.17	−30:23:49.56		
11.1	00:14:21.93	−30:24:13.89	[0.6–6.0]	2.88 ± 0.16
11.2	00:14:23.34	−30:24:05.23		
11.3	00:14:19.87	−30:24:32.09		
11.4	00:14:22.69	−30:24:23.55		
12.1	00:14:22.47	−30:24:16.09	[0.6–6.0]	4.77 ± 0.32
12.2	00:14:22.38	−30:24:11.72		
12.3	00:14:22.70	−30:24:10.76		
12.4	00:14:19.07	−30:24:35.83		
13.1	00:14:22.17	−30:24:09.21	[0.6–6.0]	1.51 ± 0.05
13.2	00:14:22.51	−30:24:07.79		
13.3	00:14:19.87	−30:24:28.96		
14.1	00:14:21.54	−30:23:40.69	[0.6–6.0]	3.86 ± 0.84
14.2	00:14:21.23	−30:23:39.97		
15.1	00:14:19.14	−30:21:27.83	[0.6–6.0]	5.82 ± 0.69
15.2	00:14:18.99	−30:21:28.25		
16.1	00:14:13.57	−30:22:32.91	[0.6–6.0]	4.70 ± 0.58
16.2	00:14:13.53	−30:22:36.36		
16.3	00:14:13.10	−30:22:45.51		
18.1	00:14:21.78	−30:23:44.02	[0.6–6.0]	3.37 ± 0.69
18.2	00:14:21.21	−30:23:44.29		

3.2.5 AS1063

We have obtained spectroscopy of images 1.1 and 1.2 using multi-object spectroscopy with Magellan/LDSS3 on the night of 2009 October 11. We used LDSS3 with 1.0 arcsec-width slits and the VPH-All grism, which altogether provide a resolution of 650 and a dispersion of 1.9 Å pixel^{-1} while covering the wavelength range 3800–9900 Å. The seeing was good (0.7–0.9 arcsec) during the 5.4 ks total exposure time of these observations. The LDSS3 spectra were calibrated, combined and extracted using standard IRAF and IDL routines. Both images AS1063-1.1 and 1.2 show a strong emission line at wavelength 8307 Å and other fainter emission lines, compatible with [O II] and [Ne III] at a spectroscopic redshift $z = 1.229 \pm 0.005$.

Additional spectroscopy was obtained on VLT/FORS2 the night of 2013 August 21, as part of the ESO programme 291.A-5027 (PI:Richard). We designed a multislit spectroscopic mask covering images 2.1, 3.1, 4.3, 6.2, 6.3, 6.4 in the strong-lensing region and we obtained 4.5 ks of exposure time under bright time but good

Table 2. As Table 1 but for MACS J0416.

ID	α (deg)	δ (deg)	$z_{\rm prior}$	$z_{\rm model}$
1.1	04:16:09.78	−24:03:41.73	1.896	
1.2	04:16:10.43	−24:03:48.75	1.896	
1.3	04:16:11.36	−24:04:07.21	1.896	
2.1	04:16:09.88	−24:03:42.77	1.8925	
2.2	04:16:10.32	−24:03:46.93	1.8925	
2.3	04:16:11.39	−24:04:07.86	1.8925	
3.1	04:16:07.39	−24:04:01.62	1.9885	
3.2	04:16:08.46	−24:04:15.53	1.9885	
3.3	04:16:10.04	−24:04:32.56	1.9885	
4.1	04:16:07.40	−24:04:02.01	[0.6–6.0]	2.04 ± 0.08
4.2	04:16:08.44	−24:04:15.53		
4.3	04:16:10.05	−24:04:33.08		
5.2	04:16:07.84	−24:04:07.21	[0.6–6.0]	1.72 ± 0.20
5.3	04:16:08.04	−24:04:10.01		
7.1	04:16:09.55	−24:03:47.13	2.0854	
7.2	04:16:09.75	−24:03:48.82	2.0854	
7.3	04:16:11.31	−24:04:15.99	2.0854	
8.1	04:16:08.78	−24:03:58.05	[0.6–6.0]	3.19 ± 1.96
8.2	04:16:08.84	−24:03:58.83		
9.1	04:16:06.49	−24:04:42.90	[0.6–6.0]	2.73 ± 0.47
9.2	04:16:06.61	−24:04:44.78		
10.1	04:16:06.24	−24:04:37.76	2.2982	
10.2	04:16:06.83	−24:04:47.12	2.2982	
10.3	04:16:08.81	−24:05:02.04	2.2982	
11.1	04:16:09.41	−24:04:13.32	[0.6–6.0]	1.08 ± 0.04
11.2	04:16:09.20	−24:04:11.11		
11.3	04:16:08.29	−24:03:57.69		
12.1	04:16:09.23	−24:04:25.74	[0.6–6.0]	1.63 ± 0.24
12.2	04:16:09.01	−24:04:23.72		
13.1	04:16:06.62	−24:04:22.03	3.2226	
13.2	04:16:07.71	−24:04:30.61	3.2226	
13.3	04:16:09.68	−24:04:53.56	3.2226	
14.1	04:16:06.30	−24:04:27.62	2.0531	
14.2	04:16:07.45	−24:04:44.26	2.0531	
14.3	04:16:08.60	−24:04:52.78	2.0531	
16.1	04:16:05.77	−24:04:51.22	[0.6–6.0]	2.09 ± 0.08
16.2	04:16:06.80	−24:05:04.35		
16.3	04:16:07.58	−24:05:08.77		
17.1	04:16:07.17	−24:05:10.91	2.2181	
17.2	04:16:06.87	−24:05:09.55	2.2181	
17.3	04:16:05.60	−24:04:53.69	2.2181	
18.1	04:16:06.26	−24:05:03.24	[0.6–6.0]	2.19 ± 0.10
18.2	04:16:06.02	−24:05:00.06		
18.3	04:16:07.42	−24:05:12.28		
23.1	04:16:10.69	−24:04:19.56	[0.6–6.0]	2.25 ± 0.11
23.2	04:16:09.50	−24:03:59.87		
23.3	04:16:08.24	−24:03:49.47		

Table 3. As Table 1 but for MACS J0717.

ID	α (deg)	δ (deg)	$z_{\rm prior}$	$z_{\rm model}$
1.1	07:17:34.86	37:44:28.39	2.963	
1.2	07:17:34.51	37:44:24.43	2.963	
1.3	07:17:33.82	37:44:17.91	2.963	
1.4	07:17:32.23	37:44:13.14	2.963	
1.5	07:17:37.39	37:45:40.90	2.963	
2.1	07:17:34.26	37:44:27.78	[0.6–6.0]	3.14 ± 1.12
2.2	07:17:33.69	37:44:21.30		
3.1	07:17:35.64	37:44:29.44	1.855	
3.2	07:17:34.66	37:44:21.11	1.855	
3.3	07:17:37.70	37:45:13.86	1.855	
4.1	07:17:31.44	37:45:01.57	1.855	
4.2	07:17:30.32	37:44:40.72	1.855	
4.3	07:17:33.83	37:45:47.80	1.855	
5.2	07:17:30.69	37:44:34.19	[0.6–6.0]	4.28 ± 0.27
5.1	07:17:31.17	37:44:48.74		
5.3	07:17:36.00	37:46:02.77		
6.1	07:17:27.43	37:45:25.59	2.393	
6.2	07:17:27.04	37:45:09.93	2.393	
6.3	07:17:29.73	37:46:11.21	2.393	
7.1	07:17:27.97	37:45:58.90	[0.6–6.0]	1.83 ± 0.56
7.2	07:17:27.61	37:45:50.88		
8.1	07:17:27.98	37:46:10.83	[0.6–6.0]	2.98 ± 0.19
8.2	07:17:26.89	37:45:47.43		
8.3	07:17:25.55	37:45:06.70		
12.1	07:17:32.44	37:45:06.82	1.699	
12.2	07:17:30.62	37:44:34.52	1.699	
12.3	07:17:33.89	37:45:38.39	1.699	
13.1	07:17:32.52	37:45:02.32	2.547	
13.2	07:17:30.61	37:44:22.86	2.547	
13.3	07:17:35.08	37:45:48.21	2.547	
14.1	07:17:33.30	37:45:07.96	1.855	
14.2	07:17:31.11	37:44:22.92	1.855	
14.3	07:17:35.08	37:45:37.21	1.855	
15.1	07:17:28.25	37:46:19.26	2.405	
15.2	07:17:26.09	37:45:36.32	2.405	
15.3	07:17:25.58	37:45:16.20	2.405	
16.1	07:17:28.59	37:46:23.89	[0.6–6.0]	3.71 ± 0.30
16.2	07:17:26.05	37:45:34.51		
16.3	07:17:25.66	37:45:13.44		
17.3	07:17:25.97	37:45:12.74	[0.6–6.0]	2.79 ± 0.22
17.2	07:17:26.26	37:45:31.82		
17.1	07:17:28.65	37:46:18.58		
18.1	07:17:27.41	37:46:07.14	[0.6–6.0]	1.88 ± 0.60
18.2	07:17:26.68	37:45:51.69		
19.1	07:17:38.17	37:45:16.87	6.40	
19.2	07:17:37.86	37:44:33.87	6.40	
19.3	07:17:31.45	37:43:53.78	6.40	

seeing conditions (0.8–0.9 arcsec). We used the 600z grism, *OG*590 order filter and 1.0 arcsec-wide slits to cover the wavelength range 7200-9800 Å at a resolution ∼1500–1900 and a dispersion 1.6 Å pixel^{-1}. The FORS2 spectra were reduced using version 4.9.11 of the FORS2 data reduction software, and combined using standard IRAF and IDL routines. Both 2D and extracted spectra were visually inspected for faint emission lines and traces of continuum.

We identified a clear emission line doublet (also visible in single exposures) for images AS1063-2.1, 3.1, and 4.3, corresponding to [O II] nebular line at $z = 1.429$, 1.398, and 1.260, respectively (Fig. 9). All three slits covering system 6 (AS1063-6.2, 6.3, and 6.4) show an identical spectrum with a strong asymmetric emission line peaking at $\lambda = 8642$ Å, which is the signature of Lyman α emission at $z = 6.107$ (Fig. 9). This confirms both the association of the three images as well as the high-redshift nature of this source (see also Boone et al. 2013).

All the redshifts measured in this cluster are in perfect agreement with estimations from a preliminary model of the mass distribution.

Table 4. As Table 1 but for MACS J1149.

ID	α (deg)	δ (deg)	$z_{\rm prior}$	$z_{\rm model}$
1.1	11:49:35.28	22:23:45.63	1.480	
1.2	11:49:35.86	22:23:50.78	1.480	
1.3	11:49:36.82	22:24:08.73	1.480	
2.1	11:49:36.58	22:23:23.06	1.894	
2.2	11:49:37.46	22:23:32.94	1.894	
2.3	11:49:37.58	22:23:34.37	1.894	
3.1	11:49:33.81	22:23:59.60	2.497	
3.2	11:49:34.25	22:24:11.07	2.497	
3.3	11:49:36.31	22:24:25.85	2.497	
4.1	11:49:34.32	22:23:48.57	[0.6–6.0]	2.57 ± 0.15
4.2	11:49:34.66	22:24:02.62		
4.3	11:49:37.01	22:24:22.03		
5.1	11:49:35.94	22:23:35.02	[0.6–6.0]	2.61 ± 0.29
5.2	11:49:36.27	22:23:37.77		
5.3	11:49:37.91	22:24:12.74		
6.1	11:49:35.93	22:23:33.16	[0.6–6.0]	2.59 ± 0.27
6.2	11:49:36.43	22:23:37.89		
6.3	11:49:37.93	22:24:09.02		
7.1	11:49:35.75	22:23:28.80	[0.6–6.0]	2.54 ± 0.25
7.2	11:49:36.81	22:23:39.37		
7.3	11:49:37.82	22:24:04.47		
8.1	11:49:35.64	22:23:39.66	[0.6–6.0]	3.10 ± 0.41
8.2	11:49:35.95	22:23:42.20		
8.3	11:49:37.69	22:24:19.99		
9.1	11:49:37.24	22:25:34.40	[0.6–6.0]	4.03 ± 0.82
9.2	11:49:36.93	22:25:37.98		
9.3	11:49:36.78	22:25:38.00		
10.1	11:49:37.07	22:25:31.83	[0.6–6.0]	4.13 ± 0.66
10.2	11:49:36.87	22:25:32.26		
10.3	11:49:36.53	22:25:35.80		
13.1	11:49:36.89	22:23:52.03	[0.6–6.0]	1.31 ± 0.04
13.2	11:49:36.68	22:23:47.96		
13.3	11:49:36.01	22:23:37.89		
14.1	11:49:34.00	22:24:12.61	[0.6–6.0]	2.85 ± 0.58
14.2	11:49:33.80	22:24:09.45		

3.2.6 Abell 370

We targeted the core of this cluster in a VLT/FORS2 spectroscopic programme meant to estimate cosmological parameters from strongly lensed features (Jullo et al. 2010). Nine multiply imaged systems were observed in MOS mode during a total of 7.5 h exposure time in the nights between 2011 September 22 and 26 (ESO programme 087.A-0326(A), PI: Jullo). We have used 1 arcsec-width slits with the GRIS300V grism (2.5 h exposure time) to search for Ly α emission or other UV features, and the GRIS600z grism and *OG*590 filter (5 h exposure time) to detect objects in the redshift range $1 < z < 2$. The dispersion per pixel is 1.63 Å in the red, and 3.3 Å in the blue. Among the strongly lensed sources targeted, we were able to measure the redshifts of image A370-6.3 at $z = 1.063$, through a clear detection of the [O II] doublet. We also detect faint emission lines for image 3.1 and 3.2, which would correspond to [O II] and [Ne III] at $z = 1.421$, and a faint emission line for image 4.1 at $z = 1.275$ with the blue grism. The redshifts measured for

Table 5. As Table 1 but for Abell S1063.

ID	α (deg)	δ (deg)	$z_{\rm prior}$	$z_{\rm model}$
1.1	22:48:46.68	−44:31:37.19	1.235	
1.2	22:48:47.02	−44:31:44.27	1.235	
1.3	22:48:44.75	−44:31:16.31	1.235	
2.1	22:48:41.81	−44:31:41.96	1.429	
2.2	22:48:42.21	−44:31:57.19	1.429	
2.3	22:48:45.24	−44:32:23.93	1.429	
3.1	22:48:45.08	−44:31:38.33	1.398	
3.2	22:48:43.01	−44:31:24.93	1.398	
3.3	22:48:46.36	−44:32:11.54	1.398	
4.1	22:48:46.25	−44:31:52.09	1.260	
4.2	22:48:46.13	−44:31:47.78	1.260	
4.3	22:48:43.17	−44:31:17.64	1.260	
5.1	22:48:42.02	−44:32:27.69	[0.6–6.0]	2.30 ± 0.10
5.2	22:48:41.56	−44:32:23.94		
5.3	22:48:39.74	−44:31:46.31		
6.1	22:48:45.37	−44:31:48.06	6.107	
6.2	22:48:45.81	−44:32:14.86	6.107	
6.3	22:48:43.45	−44:32:04.66	6.107	
6.4	22:48:41.11	−44:31:11.41	6.107	
7.1	22:48:42.92	−44:32:09.16	[0.6–6.0]	3.10 ± 0.14
7.2	22:48:44.98	−44:32:19.32		
7.3	22:48:40.96	−44:31:19.55		
8.1	22:48:46.01	−44:31:49.92	[0.6–6.0]	2.33 ± 0.08
8.2	22:48:46.21	−44:32:03.94		
8.3	22:48:42.22	−44:31:10.75		
9.1	22:48:43.28	−44:32:27.02	[0.6–6.0]	2.34 ± 0.10
9.2	22:48:41.94	−44:32:18.91		
9.3	22:48:40.27	−44:31:34.63		
10.1	22:48:39.90	−44:32:01.16	[0.6–6.0]	2.30 ± 0.13
10.3	22:48:42.68	−44:32:35.07		
11.1	22:48:44.60	−44:32:19.90	[0.6–6.0]	3.56 ± 0.19
11.2	22:48:42.92	−44:32:12.25		
11.3	22:48:40.75	−44:31:19.12		
12.1	22:48:41.32	−44:32:11.83	[0.6–6.0]	3.46 ± 0.40
12.2	22:48:44.35	−44:32:31.42		
13.1	22:48:40.66	−44:31:38.02	[0.6–6.0]	1.75 ± 0.05
13.2	22:48:41.82	−44:32:13.59		
13.3	22:48:43.65	−44:32:25.79		
14.1	22:48:43.21	−44:32:18.35	[0.6–6.0]	1.02 ± 0.02
14.2	22:48:42.13	−44:32:09.38		
14.3	22:48:41.26	−44:31:48.90		

Table 6. As Table 1 but for Abell 370.

ID	α (deg)	δ (deg)	$z_{\rm prior}$	$z_{\rm model}$
1.1	02:39:52.10	−01:34:37.28	0.806	
1.2	02:39:54.31	−01:34:34.13	0.8060	
1.3	02:39:52.48	−01:34:36.22	0.8060	
2.1	02:39:53.73	−01:35:03.58	0.7250	
2.2	02:39:53.04	−01:35:06.68	0.7250	
2.3	02:39:52.50	−01:35:04.64	0.7250	
2.4	02:39:52.66	−01:35:05.39	0.7250	
2.5	02:39:52.71	−01:35:05.81	0.7250	
3.1	02:39:51.76	−01:34:01.13	[0.6–6.0]	1.52 ± 0.06
3.2	02:39:52.45	−01:33:57.38		
3.3	02:39:54.55	−01:34:02.28		
4.1	02:39:55.12	−01:34:35.41	[0.6–6.0]	1.34 ± 0.03
4.2	02:39:52.97	−01:34:35.09		
4.3	02:39:50.87	−01:34:40.97		
5.1	02:39:53.64	−01:35:21.07	[0.6–6.0]	1.30 ± 0.05
5.2	02:39:53.08	−01:35:21.67		
5.3	02:39:52.52	−01:35:20.92		
6.1	02:39:52.68	−01:34:38.32	1.063	
6.2	02:39:51.45	−01:34:41.52	1.063	
6.3	02:39:55.12	−01:34:38.12	1.063	
7.1	02:39:52.75	−01:34:49.90	[0.6–6.0]	4.94 ± 1.17
7.2	02:39:52.77	−01:34:51.09		
8.1	02:39:51.48	−01:34:11.67	[0.6–6.0]	3.78 ± 0.66
8.2	02:39:50.86	−01:34:25.67		
9.1	02:39:50.98	−01:34:40.85	[0.6–6.0]	1.64 ± 0.04
9.2	02:39:52.68	−01:34:34.94		
9.3	02:39:55.69	−01:34:36.01		
11.1	02:39:51.32	−01:34:10.12	[0.6–6.0]	5.93 ± 0.15
11.2	02:39:50.59	−01:34:27.36		
12.1	02:39:52.74	−01:34:00.43	[0.6–6.0]	4.59 ± 0.44
12.2	02:39:50.21	−01:34:31.50		
12.3	02:39:56.19	−01:34:15.70		
13.1	02:39:55.09	−01:34:18.81	[0.6–6.0]	5.97 ± 0.33
13.2	02:39:54.05	−01:34:08.02		

systems 4 and 6 agree with the lens model predictions. However, the redshift of system 3 gives a very large χ^2 to this system. Therefore, we preferred not to use the two most uncertain redshifts (systems 3 and 4) as constraints in our lens model (Table 6). Additional follow-up spectroscopy would help us confirm these two redshifts.

3.3 Weak-lensing constraints

The background galaxy catalogues for the six clusters were derived following the method presented in (Jauzac et al. 2012, hereafter J12). Therefore, we here give a brief summary of the different steps.

The weak-lensing analysis is based on shape measurements in the ACS/*F*814*W* band. Following a method developed for the analysis of data obtained for the COSMOS survey, and described in (Leauthaud et al. 2007, hereafter L07), the SExtractor photometry package (Bertin & Arnouts 1996) is used for the detection of the sources, using the *'Hot–Cold'* method (Rix et al. 2004; L07). This detection configuration combines an optimal detection of the brightest objects (*cold* step), and of the faintest ones (*hot* step). The resulting catalogue is then cleaned by removing spurious, duplicate detections, and any sources in the vicinity of stars or saturated pixels. The star–galaxy classification is performed using a standard MAG_AUTO-MU_MAX plane selection (see L07 & J12 for more details). Finally, to overcome the pattern-dependent correlations introduced by the drizzling process between neighbouring pixels, which artificially reduce the noise level of co-added drizzled images, we apply the remedy used by L07: simply scaling up the noise level in each pixel by the same constant $F_A \approx 0.316$, defined by Casertano et al. (2000).

Since only galaxies behind the clusters are gravitationally lensed, the presence of cluster members dilutes the observed shear and reduces the significance of all quantities derived from it (see J12 for a more detailed discussion). Therefore, the identification and the removal of the contaminating unlensed galaxies is crucial. Thanks to the existing *HST* data for all six clusters, a minimum of two colours is available for each of them. Therefore, following the methodology described in J12, we used the existing spectroscopic and photometric redshifts (Owers et al. 2011; Ebeling, Ma & Barrett 2014) to calibrate a colour–colour selection to identify the foreground galaxies and cluster members (the combination of filters used for each cluster is given in Table 7).

The measure of galaxy shapes is done using the RRG method (Rhodes, Refregier & Groth 2000), which was developed for the

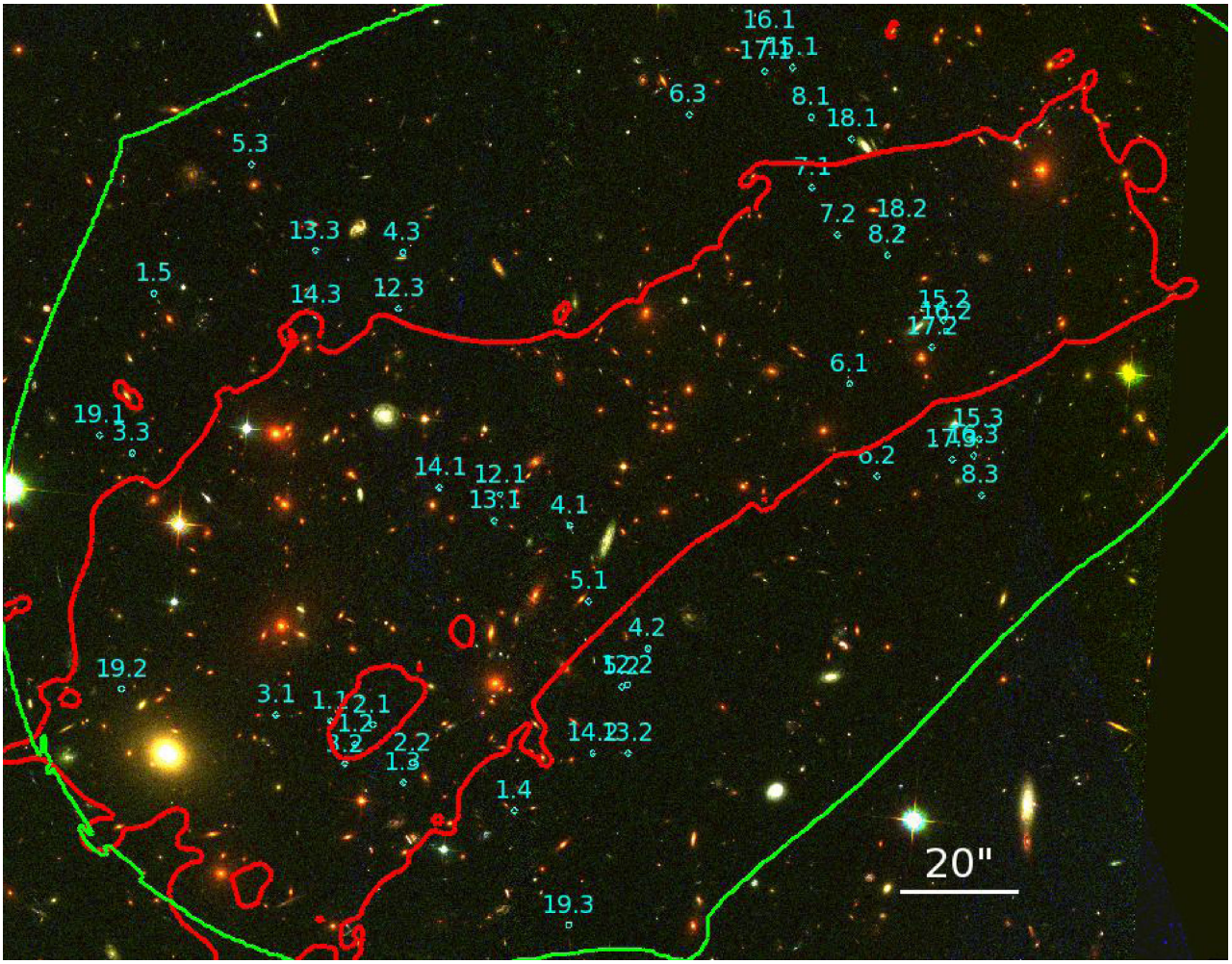

Figure 5. Same as Fig. 2 but for MACS J0717 and filter combination *F*435*W*+*F*555*W*+*F*814*W*.

analysis of data obtained from space, and is thus ideally suited for use with a small, diffraction-limited point spread function (PSF) as it decreases the noise on the shear estimators by correcting each moment of the PSF linearly, and only dividing them at the very end to compute an ellipticity. The last step of the weak-lensing catalogue construction consists of applying lensing cuts, i.e. to exclude galaxies whose shape parameters are ill-determined, and will thus increase the noise in the shear measurements more than add to the shear signal. More details can be found in J12. Finally, we assume the redshift distribution of Smail & Dickinson (1995) for the background galaxies with shear measurement. The final density of background galaxies we obtained for each clusters are given in Table 7.

4 METHODOLOGY

We combine strong-lensing and weak-lensing constraints to model the mass distribution in each cluster. Following our successful strategy from previous lensing work (e.g. Limousin et al. 2007, 2012; Richard et al. 2010a,b), we adopt a parametric model combining both large-scale (cluster or group size) mass clumps as well as galaxy-scale mass clumps. In the following, we describe the selection of cluster members across the ACS field of view, the choice of model parameters, and their optimization.

4.1 Galaxy catalogues

We create object catalogues for each HFF cluster using SExtractor (Bertin & Arnouts 1996) for the areas shown in Fig. 1, i.e. the region within which *HST* imaging data are available in at least three well separated passbands. Using the *F*606*W* images (*F*625*W* in the case of A370) as the primary detection band, we run SExtractor in dual-image mode on the images in each passband. The resulting catalogues are combined to create for each cluster a master catalogue of objects. Star–galaxy separation is performed by identifying stars in two separate parameter spaces, namely peak surface brightness versus flux, and half-light radius versus flux. We remove from our catalogues all stars and all spurious sources found either to feature a higher peak surface brightness or to be more compact than stars. To improve the robustness of this procedure (the small area covered by the existing *HST* images of the HFF contains very few stars for each individual field), we perform the star–galaxy separation on a combined object catalogue for all six fields.

The resulting catalogues of galaxies are then used to establish colour–colour cuts for the identification of likely cluster members. We examine the distribution of galaxies in both colour–magnitude diagrams and in colour–colour space ($m_{F435W} - m_{F606W}$ versus $m_{F606W} - m_{F814W}$), highlighting the loci of spectroscopically confirmed cluster members. We then define probable cluster members

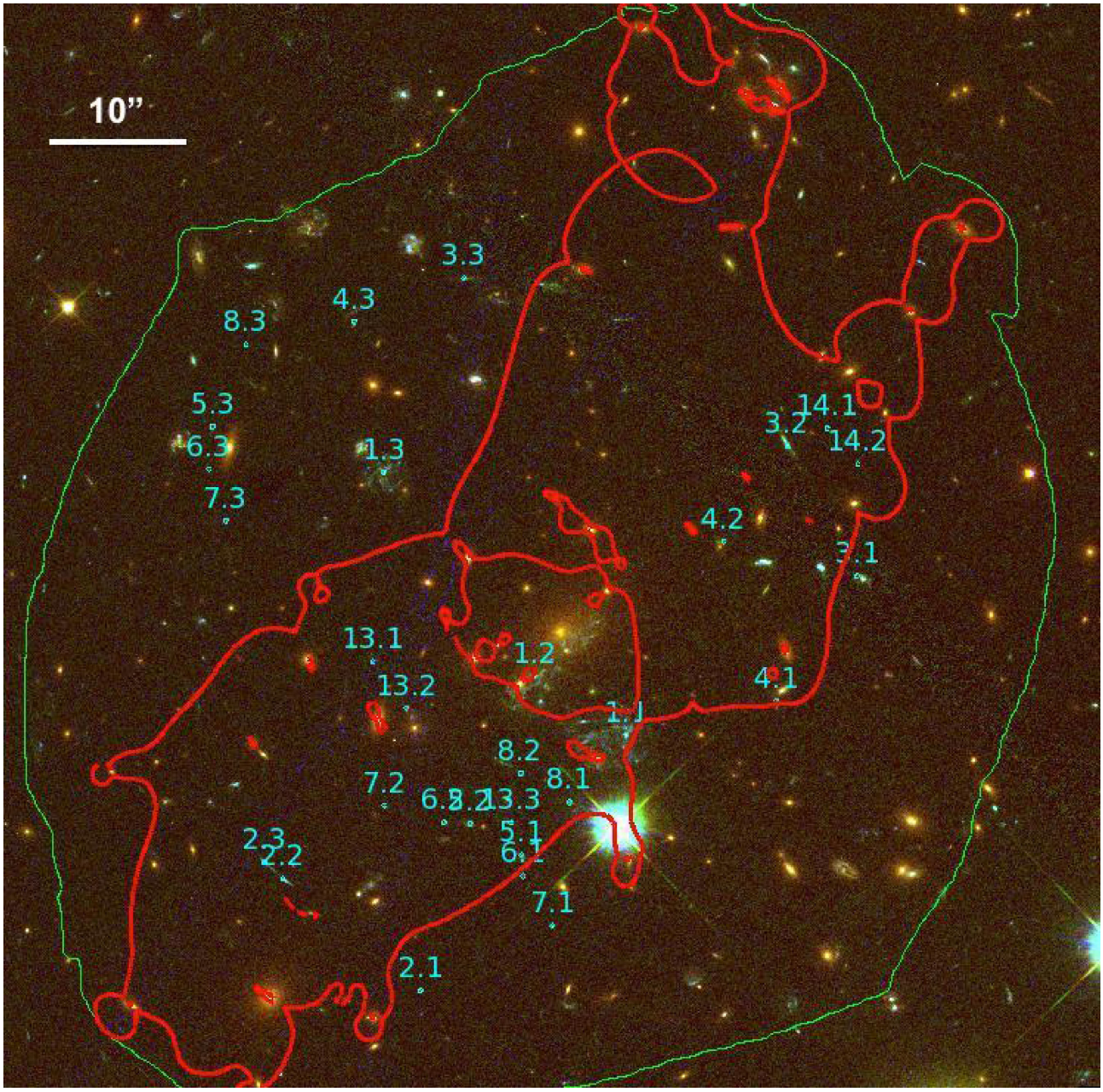

Figure 6. Same as Fig. 2 but for MACS J1149 and filter combination $F435W$+$F555W$+$F814W$.

to be those galaxies that fall within 3σ of a linear model of the cluster red sequence in both the $(m_{F606W} - m_{F814W})$ versus m_{F814W} and the $(m_{F435W} - m_{F606W})$ versus m_{F814W} colour–magnitude diagrams. Fig. 10 shows the galaxies selected by this process as well as all spectroscopically confirmed cluster members. We compile the latter from various catalogues of spectroscopic redshifts: for A2744, we consult Owers et al. (2011); for MACS J0416, MACS J0717, and MACS J1149, we use the redshifts published by Ebeling et al. (2014); and for AS1063 and A370, we rely on spectroscopic redshifts compiled in the NASA Extragalactic Database. We also use redshifts obtained by Balestra et al. (2013, in preparation) for MACS J0416. As shown in Fig. 10, the galaxies selected by the dual red-sequence criterion fall into a well-defined triangular region of $(m_{F435W} - m_{F606W})$ versus $(m_{F606W} - m_{F814W})$ colour–colour space. Galaxies featuring luminosities exceeding $M_{F814W} = 0.01\,L^*$ are included in our strong-lensing mass model as small-scale perturbers (see following section).

4.2 Model parametrization

Producing a magnification map involves solving the lens equation for light rays originating from distant sources and deflected by the massive foreground cluster. This is ultimately an inversion problem for which several sets of codes and approaches have been developed independently. Our collaboration uses LENSTOOL[2] (Jullo et al. 2007), an algorithm we developed collectively over the years. In this software, the cluster mass distribution can be described as a combination

[2] Publically available on the dedicated web page

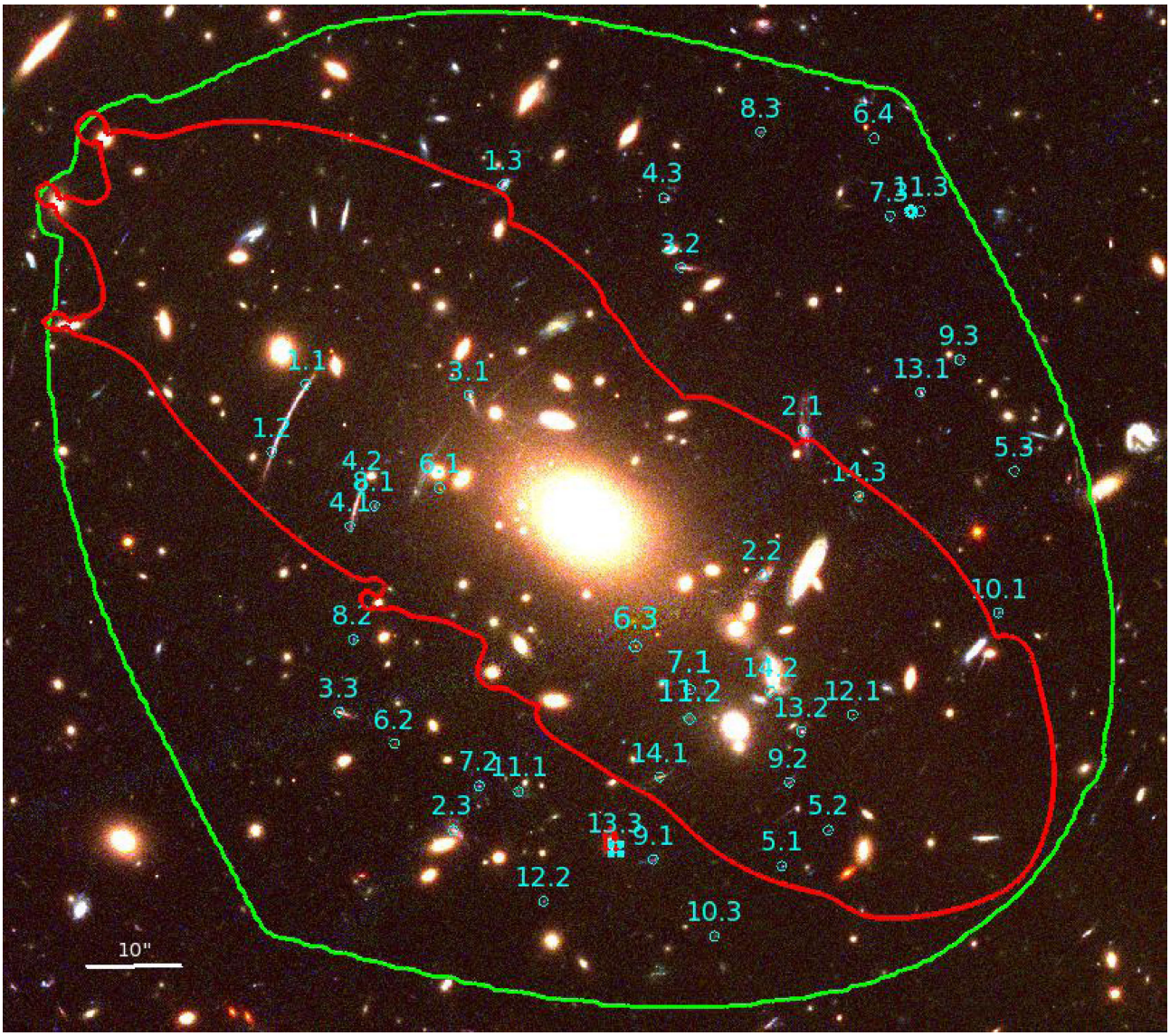

Figure 7. Same as Fig. 2 but for Abell S1063 and filter combination *F*606*W*+*F*814*W*+*F*160*W*.

of physically motivated mass components, both for the individual galaxies and the smoother, large-scale haloes.

As a basis function for our models, we adopt the dual pseudo-isothermal elliptical mass distribution (dPIE, also known as truncated PIEMD), which corresponds to an isothermal profile with two characteristic radii: a core radius $r_{\rm core}$ (producing a flattening of the mass distribution at the centre), and a cut radius $r_{\rm cut}$ (producing a drop-off of the mass distribution on large scales). More details on the dPIE parametrization are given in Richard et al. (2009) and Limousin et al. (2012).

This method has the advantage that the geometrical parameters of the galaxy-scale components (centre, ellipticity, orientation) can be directly related to the shape parameters measured from the light distribution of cluster galaxies in our photometric catalogue. In order to limit the number of free parameters in our model, we use the *F*814*W* band as the reference band for these shape measurements and determine the three other parameters of each galaxy's dPIE description (central velocity dispersion σ, core, and cut radii) from scaling relations based on the galaxy's luminosity L relative to L^*. We set $r^*_{\rm core} = 0.15$ kpc for all models, but optimize both σ^* and $r^*_{\rm cut}$, following Smith et al. (2009) and Limousin et al. (2012), respectively. We adopt a flat prior for $r^*_{\rm cut}$ in the range [1−100] kpc, and a Gaussian prior $\sigma^* = 158 \pm 27$ km s^{-1}, as demonstrated by Richard et al. (2010b) for a sample of $z \sim 0.2$ clusters.

At present, the prevailing modelling approach is to assign a small-scale dark matter clump to each cluster galaxy in our catalogue, and a large-scale dark matter clump to prominent concentrations of cluster galaxies. This technique has proven very reliable and provides results in mass distributions in reasonably good agreement with theoretical predictions from high-resolution cosmological *N*-body simulations (Natarajan & Kneib 1997; Natarajan, De Lucia & Springel 2007). This explicit one-to-one correspondence between mass and light is less accurate, however, in the outer regions of clusters where the galaxy distribution is sparser, and strong-lensing constraints are unavailable. The solution is to combine strong-lensing constraints near the cluster cores with a weak-lensing analysis on larger scales.

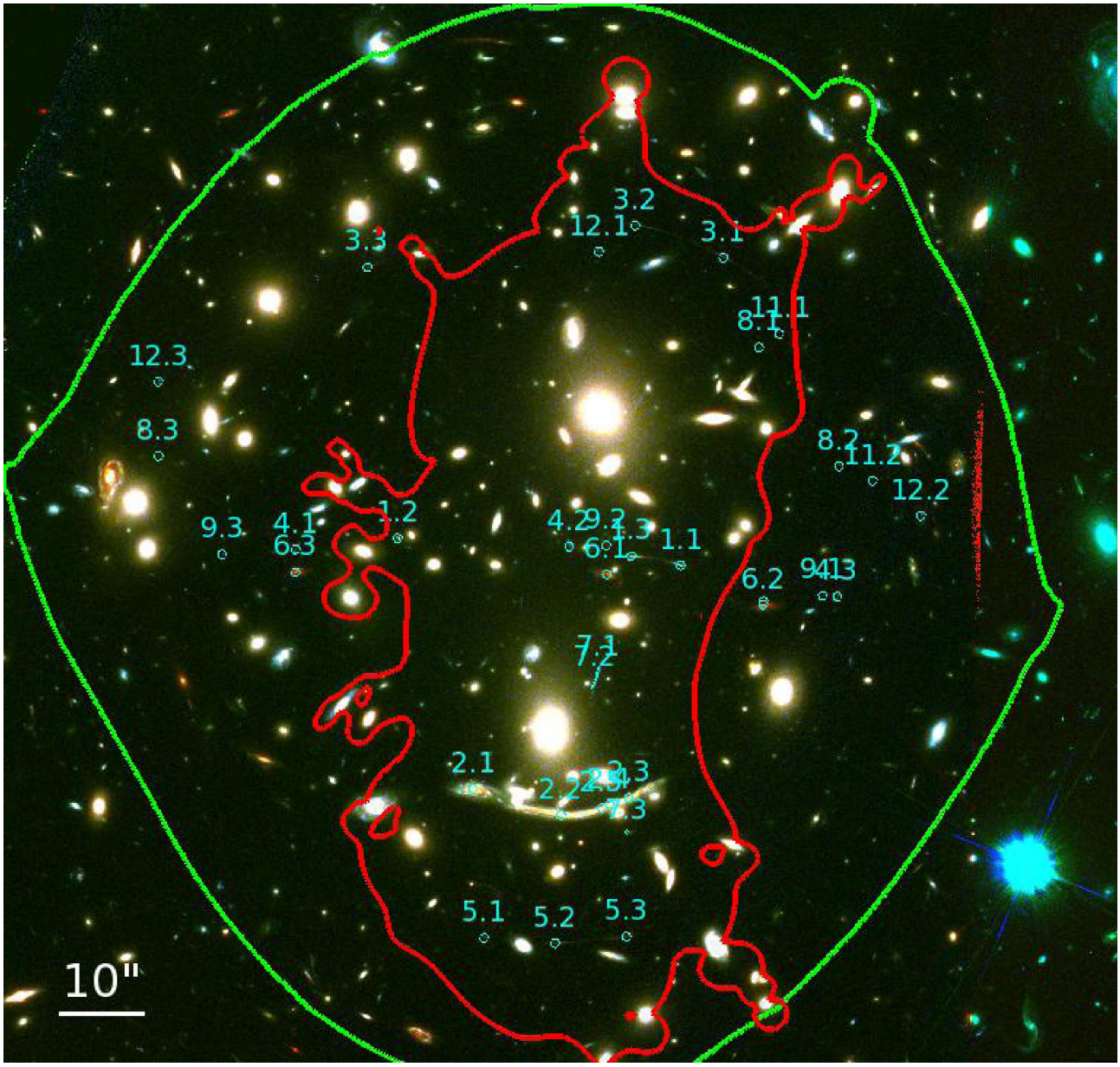

Figure 8. Same as Fig. 2 but for Abell 370 and filter combination *F*625*W*+*F*814*W*+*F*160*W*.

4.3 Likelihoods definition

For each Frontier Field cluster, we optimize two parametric models: an SL (strong-lensing) model solely based on the strong-lensing constraints presented in Section 3.1, and an SL+WL model combining the strong-lensing constraints with a weak-lensing analysis, as described in Section 4.3. We proceed in two steps for each cluster: we start by creating an SL model, optimized in the image plane, and determine the parametrization (number of clumps and individual galaxies to be optimized). In this case, we used the following likelihood definition

$$\mathcal{L}_{\rm SLimg} = \prod_{i,j}^{M,N_i} \frac{1}{\sqrt{2\pi\sigma_{\rm SL}^2}} \exp\left(-\frac{1}{2}\frac{|\theta_{ij} - \langle\theta_i\rangle|^2}{\sigma_{\rm SL}^2}\right), \quad (1)$$

where $\langle\theta_i\rangle$ is the estimated image position for system i, based on the barycentre of the multiple positions in the source plane.

We then use the same parametrization to optimize the SL+WL model, this time performing the optimization in the source plane which is less computing-time intensive. To this end, we define the total likelihood $\mathcal{L} = \mathcal{L}_{\rm SLsrc} \times \mathcal{L}_{\rm WL}$ as the product of the strong- and the weak-lensing likelihoods. The strong-lensing likelihood in the source plane is, in turn, defined as the product of M systems of N_i multiple-image likelihoods

$$\mathcal{L}_{\rm SLsrc} = \prod_{i,j}^{M,N_i} \frac{1}{\sqrt{2\pi\mu_{ij}^{-1}\sigma_{\rm SL}^2}} \exp\left(-\frac{1}{2}\frac{|\beta_{ij} - \langle\beta_i\rangle|^2}{\mu_{ij}^{-1}\sigma_{\rm SL}^2}\right), \quad (2)$$

where β_{ij} are the source positions of the multiple images, and $\langle\beta_i\rangle$ are the barycentre of these positions for system i. For each image, the positional uncertainty in the image-plane $\sigma_{\rm SL}$ is multiplied by the amplification μ_{ij}. We conduct this optimization in the source plane as the much more involved computations of an image-plane optimization would have unduly strained the available computing

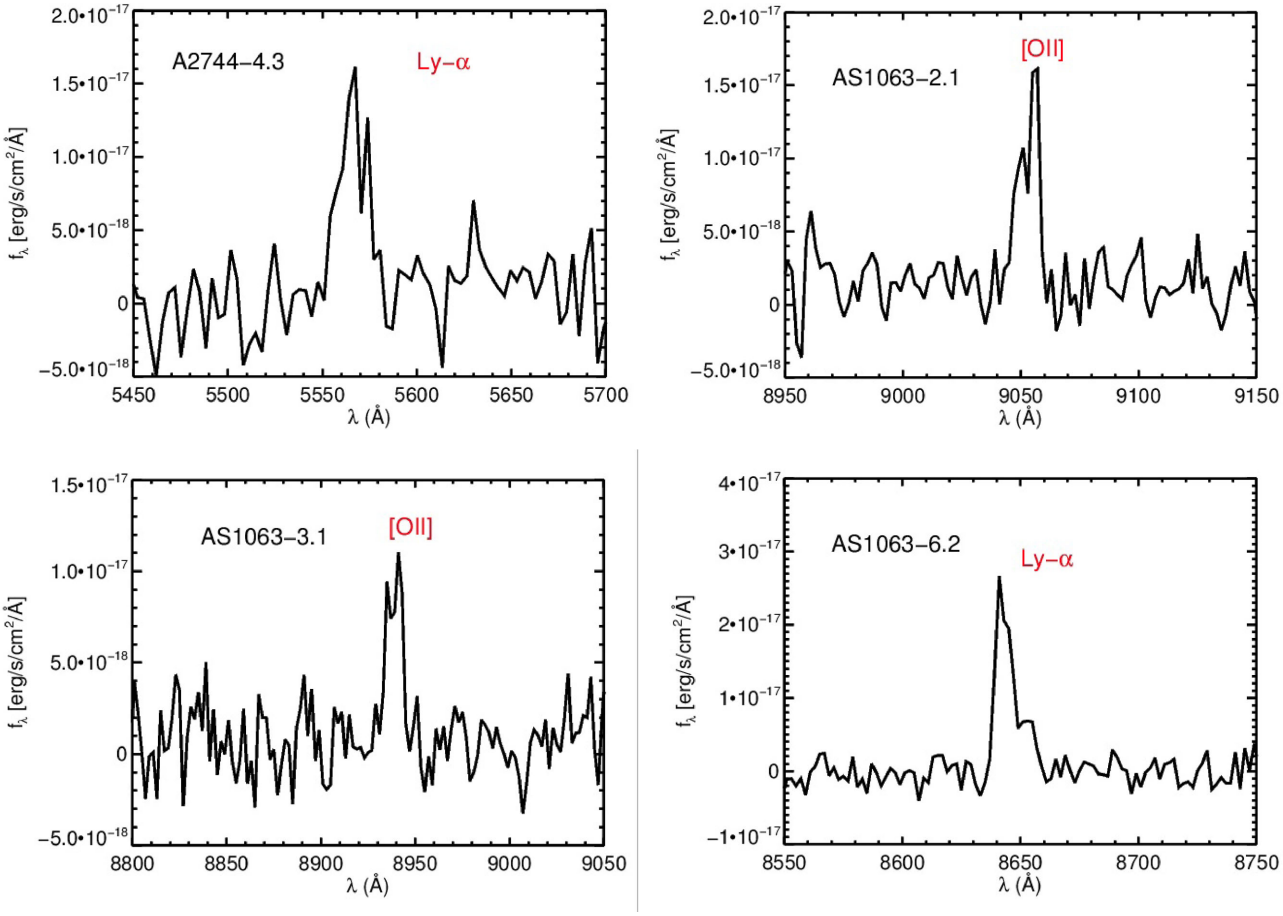

Figure 9. Example of extracted spectra showing identified emission lines in multiple images.

Table 7. Weak-lensing background galaxy densities obtained for each HFF cluster, as well as the *HST*-ACS filters used for the colour–colour selection to identify foreground galaxies and cluster members.

Target	Colour–colour selection	Density of background sources
A2744	*F*435*W*–*F*606*W*–*F*814*W*	61 gal arcmin^{-2}
MACSJ0416.1−2403	*F*475*W*–*F*625*W*–*F*814*W*	50 gal arcmin^{-2}
MACSJ0717.5+3745	*F*475*W*–*F*625*W*–*F*814*W*	51 gal arcmin^{-2}
MACSJ1149.5+2223	*F*475*W*–*F*625*W*–*F*814*W*	61 gal arcmin^{-2}
AS1063	*F*475*W*–*F*625*W*–*F*814*W*	64 gal arcmin^{-2}
A370	*F*475*W*–*F*625*W*–*F*814*W*	74 gal arcmin^{-2}

resources. We find that, for strong-lensing data sets only, source- and image-plane optimizations yield similar reconstructions for the clusters studied in this work.

Finally, the weak-lensing likelihood is defined as the product of the L weak-lensing source likelihoods

$$\mathcal{L}_{\rm WL} = \prod_i^L \frac{1}{\sqrt{2\pi\sigma_{\epsilon_i}^2}} \exp\left(-\frac{1}{2}\frac{|\epsilon_i^s|^2}{\sigma_{\epsilon_i}^2}\right), \quad (3)$$

where $|\epsilon_i^s|$ is the module of the predicted source ellipticity obtained from the amplification matrix $\mathbf{A}$ and the second brightness moments of each image $\mathbf{Q}$, through the equation $\mathbf{Q}_i^s = \mathbf{AQA}^T$ (Bartelmann 2001). The ellipticity is defined as $e = (a^2 - b^2)/(a^2 + b^2)$, where a and b are the eigenvalues of $\mathbf{Q}$. This matrix transformation is valid both in the weak- and in the strong-lensing regime. In this work, we assume $\sigma_{\epsilon_i}^2 = \sigma_{\rm int}^2 + \sigma_{{\rm meas}_i}^2$, i.e. the variance is the quadratic sum of the intrinsic ellipticity and the shape measurement errors for each galaxy.

By adopting this two-step approach, we avoid the possibility of reaching a local minimum in the source-plane optimization: in the SL+WL model, group- and cluster-scale haloes are mainly optimized on large scales based on weak-lensing constraints, while their centre and shape parameters remain similar to those of the SL model.

5 RESULTS

5.1 Parametric model

The number of large-scale clumps included in each cluster was chosen to minimize the number of free parameters while reproducing

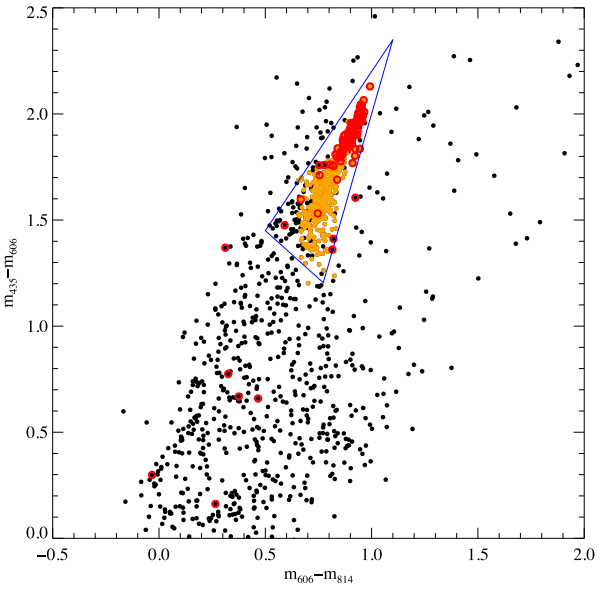

Figure 10. Colour–colour diagram for galaxies in the A2744 field, as defined in Fig. 1. Galaxies marked in orange meet the dual red-sequence criterion, i.e. they fall within 3σ of the cluster red sequence in both the ($m_{F606W} - m_{F814W}$) versus m_{F814W} and the ($m_{F435W} - m_{F606W}$) versus m_{F814W} colour–magnitude diagrams. Galaxies highlighted in red are spectroscopically confirmed cluster members.

the multiple-image sets to an accuracy of better than 0.8 arcsec. The number of large-scale clumps finally adopted for our models varies from 1 (for Abell S1063) to 5 (for Abell 2744 and MACS J0717). As shown in Section 3.1, Abell 2744 features a bimodal mass distribution on large scales, but also includes a number of group-scale structures at the edges of the ACS field of view. For the even more complex system MACS J0717, the distribution of cluster light shows peaks at the location of each large-scale clump (see the discussion in Limousin et al. 2012).

In addition to these large-scale haloes, a few individual galaxies are explicitly included in our lens models, as their adopted properties have a strong influence on the location of nearby multiple-imaged systems. This is true for two galaxies in Abell 2744, two galaxies in Abell 370 (as already found by Richard et al. 2010a), as well as for a massive foreground galaxy at $z \sim 0.1$ in the field of MACS J0416 which does not follow the same scaling relations as the cluster members.

For each cluster, we describe the large-scale potentials (identified as DM1 to DM5), the aforementioned added galaxy-scale potentials (GAL1 and GAL2), and the scaling relations for cluster members, presented for a L* galaxy. The optimized source redshift for all multiple-image systems without spectroscopic redshift is summarized in the last column of Tables 1 to 6. The resulting parameters of the combined (SL+WL) models are summarized in Table 8. The parameters of the combined models agree with those of the best-fitting SL models within the 2σ uncertainties; the resulting $\chi 2$ values are very similar too. As expected, the most massive components detected by our weak-lensing analysis were thus already present in our SL parametrization.

5.2 Output maps and error estimation

The parametric models are adjusted with LENSTOOL in a Bayesian way, i.e. we probe their posterior probability density with a MCMC sampler (Jullo et al. 2007). This process allows us to easily and reliably estimate the errors on derived quantities such as the amplification maps and the mass maps. For each cluster, we use 200 randomly selected models to sample the posterior-probability distribution of each parameter.

High-resolution mass maps (integrated over the line of sight) were produced for each of these models, and then integrated as a function of the radial distance from their barycentre. The resulting average integrated mass and 1σ dispersion (computed over the 200 maps per cluster) are presented in Fig. 11. All FF clusters are found to be very massive, reaching integrated masses at 500 kpc radius between 4×10^{14} (for MACS J0416) and 10^{15} $M_{\odot}$ for the most massive cluster MACS J0717. At $r < 100$ kpc, all six mass profiles look very similar, the sole exception being the highly concentrated and fully relaxed system Abell S1063, whose brightest cluster galaxy is almost exactly centred within a single large-scale dark matter halo.

We applied the same procedure to create amplification maps and accompanying error maps in all six fields, assuming fiducial source redshifts of $z = 1$, 2, 4, and 9. Examples are shown in Fig. 12. These maps can also be extrapolated to the locations of the blank fields for the benefit of the larger extragalactic community. Amplification maps at other source redshifts can be derived based on the convergence κ and shear γ maps before normalization by the geometrical distance ratio between the cluster and the source. For a given image position and source redshift, one can derive the magnification μ as follows:

$$1/\mu = (1 - (D_{\rm LS}/D_{\rm S})\,\kappa)^2 - ((D_{\rm LS}/D_{\rm S})\gamma)^2, \quad (4)$$

where DLS and DS are the angular diameter distance between the lens and the source, and between the observer and the source, respectively.

The best-fitting LENSTOOL models, mass maps, amplification maps, and relative errors, as well as the 200 convergence and shear maps for each cluster, are made publicly available on the Frontier Fields website http://archive.stsci.edu/prepds/frontier/lensmodels/.

It is worth mentioning that the relative errors computed from the MCMC samples are only statistical errors and do not include systematics due to the assumptions made in the models. In order to estimate the level of these systematics, we have performed three specific tests, where we re-optimized the six mass models under different assumptions: (a) we selected only 10 robust multiple systems per cluster, i.e. either spectroscopically confirmed and/or among the brightest systems in agreement with various lensing groups, as strong-lensing constraints; (b) we increased the error measurement on the shear values by 50 per cent; and (c) we increased by $\Delta z = 0.5$ the distribution assumed for background sources in the weak-lensing constraints. By comparing the magnification maps at very high redshift, we observed an average variation in magnification within the ACS field of view by 0.1–0.35 mag for test (a), by 0.1 mag for test (b), and by 0.05–0.1 mag for test (c), depending on the complexity of the cluster model. As expected due to its strong influence on high magnification values, the robustness of multiple systems used as constraints produces the stronger systematics. This justifies the need for future comparison between the magnification maps produced by the different modelling teams on the same simulated cluster.

6 DISCUSSION

One of the key goals of the Frontier Fields initiative is to improve the statistics on faint distant galaxies observed during the epoch of reionization. The expected extent of this improvement can be

Table 8. Best-fitting parameters of the mass components in each cluster for the models optimized with the combination of strong-lensing and weak-lensing constraints. From left to right: identification of potential (DM: cluster-scale dark matter halo, GAL: galaxy-scale halo, L*: scaling relation parameters for L* galaxy in cluster members), relative astrometric position of centre of potential, ellipticity, and position angle, core, and cut radii, velocity dispersion.

Potential	$\Delta\alpha$ (arcsec)	$\Delta\delta$ (arcsec)	e	θ (deg)	$r_{\rm core}$ (kpc)	$r_{\rm cut}$ (kpc)	σ (km s^{-1})
Abell 2744, $\alpha = 00{:}14{:}20.698$, $\delta = -30{:}24{:}00.60$, $z = 0.308$							
DM1	$-7.0^{+1.0}_{-0.9}$	$-6.4^{+1.3}_{-1.3}$	$0.21^{+0.04}_{-0.05}$	$82.9^{+3.8}_{-7.9}$	107^{+12}_{-9}	[1000]	826^{+42}_{-56}
DM2	$-17.9^{+0.3}_{-0.4}$	$-18.1^{+0.4}_{-0.3}$	$0.57^{+0.04}_{-0.04}$	$43.0^{+2.1}_{-1.3}$	35^{+3}_{-2}	[1000]	621^{+26}_{-17}
DM3	[24.2]	[155.8]	[0.30]	[−74.8]	116^{+0}_{-15}	[1000]	665^{+30}_{-50}
DM4	$104.4^{+2.4}_{-1.1}$	$83.1^{+0.4}_{-1.8}$	$0.16^{+0.07}_{-0.08}$	$8.9^{+6.9}_{-3.9}$	64^{+8}_{-6}	[1000]	747^{+42}_{-34}
DM5	$0.2^{+1.0}_{-1.1}$	$20.3^{+1.0}_{-1.3}$	$0.67^{+0.01}_{-0.13}$	$126.0^{+9.9}_{-9.0}$	37^{+4}_{-3}	[1000]	439^{+46}_{-22}
GAL1	[−12.7]	[−0.8]	[0.30]	[−46.6]	[0]	[43]	6^{+29}_{-56}
GAL2	[−3.6]	[24.7]	[0.72]	[−33.0]	[0]	[34]	153^{+24}_{-69}
L* galaxy					[0.15]	7^{+2}_{-2}	167^{+5}_{-8}
MACS J0416 $\alpha = 04{:}16{:}09.144$, $\delta = -24{:}04{:}02.95$, $z = 0.396$							
DM1	$-5.6^{+1.0}_{-0.6}$	$2.7^{+0.7}_{-0.7}$	$0.71^{+0.04}_{-0.06}$	$146.5^{+1.5}_{-1.7}$	76^{+12}_{-7}	[1000]	809^{+46}_{-38}
DM2	$23.7^{+1.4}_{-0.7}$	$-45.7^{+1.5}_{-1.4}$	$0.56^{+0.04}_{-0.06}$	$128.5^{+0.8}_{-0.6}$	120^{+10}_{-7}	[1000]	1019^{+36}_{-43}
GAL1	[31.8]	[−65.5]	[0.04]	[−40.4]	[0]	[62]	[140]
L* galaxy					[0.15]	9^{+15}_{-8}	183^{+16}_{-16}
MACS J0717 $\alpha = 07{:}17{:}35.575$, $\delta = +37{:}44{:}44.57$, $z = 0.545$							
DM1	$5.0^{+1.8}_{-1.2}$	$16.2^{+2.3}_{-3.1}$	$0.59^{+0.09}_{-0.08}$	$68.9^{+6.1}_{-8.3}$	34^{+29}_{-5}	[1000]	837^{+56}_{-58}
DM2	$35.5^{+2.6}_{-1.8}$	$-10.1^{+3.1}_{-3.5}$	$0.95^{+0.04}_{-0.09}$	$49.4^{+4.8}_{-4.2}$	60^{+31}_{-18}	[1000]	719^{+89}_{-67}
DM3	$71.1^{+4.7}_{-11.3}$	$35.8^{+3.1}_{-4.1}$	$0.90^{+0.03}_{-0.04}$	$20.1^{+4.5}_{-3.0}$	154^{+49}_{-26}	[1000]	1082^{+70}_{-209}
DM4	$98.1^{+5.7}_{-9.3}$	$72.0^{+5.9}_{-5.5}$	$0.81^{+0.13}_{-0.12}$	$-24.1^{+24.4}_{-7.0}$	35^{+49}_{-28}	[1000]	521^{+138}_{-83}
DM5	[−19.4]	[−21.7]	[0.23]	[−40.0]	[2]	[392]	[180]
L* galaxy					[0.15]	67^{+12}_{-18}	135^{+25}_{-24}
MACS J1149 $\alpha = 11{:}49{:}35.695$, $\delta = +22{:}23{:}54.70$, $z = 0.544$							
DM1	$-0.8^{+1.4}_{-2.3}$	$1.4^{+1.5}_{-1.6}$	$0.63^{+0.05}_{-0.07}$	$35.1^{+2.0}_{-2.5}$	201^{+61}_{-10}	[1000]	1242^{+84}_{-84}
DM2	$-23.1^{+1.4}_{-2.5}$	$-23.7^{+1.1}_{-2.4}$	[0.00]	[34.0]	3^{+13}_{-1}	[1000]	235^{+56}_{-32}
DM3	$9.6^{+3.9}_{-1.0}$	$40.3^{+1.3}_{-0.1}$	[0.00]	[34.0]	11^{+28}_{-3}	[1000]	407^{+59}_{-48}
DM4	$-13.6^{+2.2}_{-1.4}$	$98.3^{+1.7}_{-1.9}$	[0.23]	[−66.2]	21^{+14}_{-6}	[1000]	363^{+76}_{-34}
DM5	[0.0]	[0.0]	[0.20]	[34.0]	17^{+12}_{-5}	230^{+109}_{-38}	445^{+5}_{-62}
L* galaxy					[0.15]	30^{+11}_{0}	153^{+3}_{-1}
AbellS 1063 $\alpha = 22{:}48{:}43.973$, $\delta = -44{:}31{:}51.20$, $z = 0.348$							
DM1	$0.8^{+0.4}_{-0.3}$	$0.1^{+0.3}_{-0.3}$	$0.58^{+0.01}_{-0.01}$	$-37.3^{+0.2}_{-0.2}$	120^{+3}_{-4}	[1000]	1374^{+9}_{-7}
L* galaxy					[0.15]	32^{+12}_{-2}	104^{+18}_{-24}
Abell 370 $\alpha = 02{:}39{:}53.076$, $\delta = -01{:}34{:}56.14$, $z = 0.375$							
DM1	$3.1^{+0.5}_{-0.5}$	$8.6^{+0.1}_{-0.6}$	$0.59^{+0.04}_{-0.04}$	$-106.0^{+2.8}_{-3.3}$	64^{+8}_{-5}	[1000]	833^{+58}_{-6}
DM2	$-2.5^{+0.8}_{-0.0}$	$35.6^{+1.5}_{-2.2}$	$0.38^{+0.04}_{-0.05}$	$-89.6^{+2.8}_{-2.4}$	155^{+9}_{-12}	[1000]	1128^{+37}_{-51}
GAL1	[−0.0]	[0.0]	[0.30]	[−81.9]	[0]	34^{+4}_{-3}	129^{+22}_{-22}
GAL2	[7.9]	[−9.8]	[0.26]	[25.7]	[0]	28^{+5}_{-4}	64^{+11}_{-16}
L* galaxy					[0.15]	61^{+21}_{-5}	116^{+16}_{-8}

assessed using our best models for each cluster, which yield the gravitational magnification for high-redshift galaxies in the central region covered by deep observations with both ACS and WFC3. In doing so, we adopt $z = 7$ as a reference source redshift, noting though that the change in magnification is typically very small between $z = 7$ and 10.

A first estimate of the relative lensing efficiency of the six HFF clusters can be obtained by comparing their peak magnification values. These are reached close to the *critical lines*, which are shown in red in Figs 2–8. The solid angles over which magnifications of $\mu > 5$ and $\mu > 10$ are attained in each cluster range from 0.8 to 2.9 arcmin^2 and are summarized in Table 9. While the largest areas with significant magnification are provided by MACS J0717, Abell 370, and Abell S1063, all FF clusters are similarly efficient lenses to within a factor of 2.

One shortcoming of peak magnification as a metric for measuring lensing efficiency is that it provides no information about image multiplicity, i.e. the frequency of the various lensing configurations (the creation of 1, 3, 5, or more images from a single source), which can vary from cluster to cluster. We therefore compute a second important cluster attribute, namely the sky area covered by multiple images in the image plane. This area is related to the number of multiple images expected to be found in each cluster. The sky area within which multiple images are observed encloses the critical line but has a more circular shape, covering between 1.5 and 4.2 arcmin^2 for the six HFF clusters (Table 9). Based on these figures, we expect to find multiple images of high-redshift sources across almost the entire solid angle (91 per cent) of the WFC3 pointing on MACS J0717. Again, Abell 370 and Abell S1063 show the second- and third-highest fraction of WFC3 solid angle conducive to multiple-image creation. The lower values for Abell 2744, MACS J0416, and MACS J1149 are caused by their higher elongation and orientation within the WFC3 footprint on the sky.

The combined effect of magnification and image multiplicity is best assessed in the source plane. To this end, we take advantage of LENSTOOL's capability to provide source-plane magnification maps based on, for a given source position, the most magnified image. Inverting the combined ACS+WFC3 aperture yields the

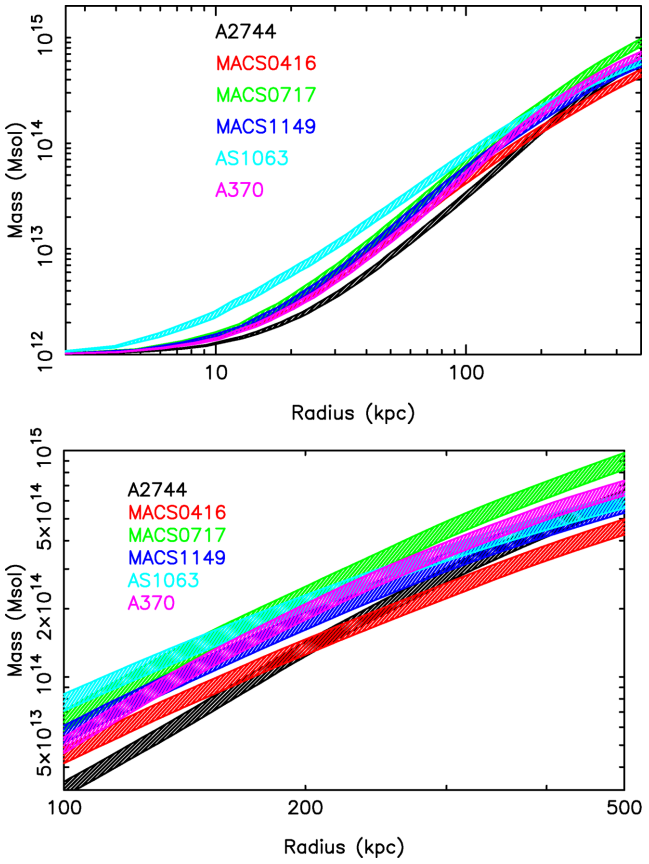

Figure 11. Total integrated mass as a function of the projected distance from the barycentre. Each colour-hatched region corresponds to the average and 1σ dispersion on the integrated mass in each FF cluster. The bottom panel shows a zoom over the $100 < r < 500$ kpc region.

Table 9. Lensing efficiency of the HFF clusters using various metrics. From left to right: fraction of the area in the image plane amplified by $\mu > 5$, by $\mu > 10$, and covered by multiple images, and the surface area in the source plane magnified by $\mu > 3$. All areas relate to the overlapping region with foreseen deep ACS and WFC3 observations.

Cluster	$\Omega_i(\mu > 5)$ (per cent)	$\Omega_i(\mu > 10)$ (per cent)	Ω_i(mult) (per cent)	$\sigma_\mu(\mu > 3)$ arcmin^2
Abell 2744	36	18	32	0.41
MACS J0416	32	17	46	0.22
MACS J0717	48	28	90	0.28
MACS J1149	38	20	39	0.28
Abell 370	61	38	65	0.28
Abell S1063	47	25	55	0.26

source-plane magnification maps shown in Fig. 13, where the regions of highest magnification now clearly delineate the *caustic lines*. The strong variation in shape and surface area of these maps directly reflects the fraction of the respective HFF field that falls within the critical line. Indeed, the total surface area in the source plane above a given magnification factor is directly proportional to the unlensed comoving volume covered at high redshift with this magnification (Fig. 14). As a result, Wong et al. (2012) proposed to use σ_μ, the total surface area in the source plane above $\mu = 3$, as a measurement of the efficiency of the lensing configuration to magnify high-redshift galaxies. These values are also reported in Table 9.

Finally, we use the recent estimates on the UV luminosity function at high redshift from Bouwens et al. (2014) to predict the number of high-redshift dropouts at $z \sim 7$, $z \sim 9$, and $z \sim 11$ expected to be detected in the FF data, as a function of their observed (lensed) magnitude (Fig. 15). We assume an unbiased selection over a redshift interval $\Delta z = 1$ centred on each redshift. The predictions at $z \sim 9$ and $z \sim 11$ use the fitting formula given by Bouwens et al. (2014) for the evolution of the Schechter (1976) parameters of the luminosity function at high redshift.

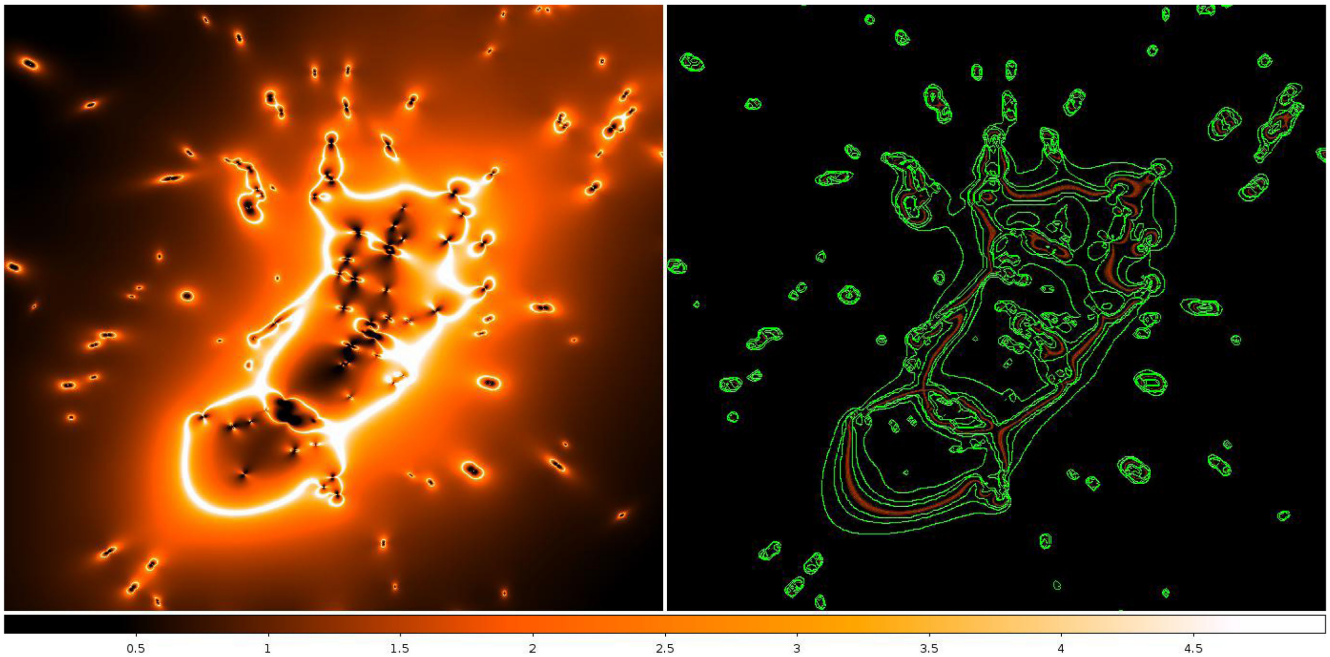

Figure 12. Magnification map (left-hand panel) and error map (right-hand panel) produced in the central region of Abell 2744 for a source at $z = 9$. Contours show a relative error of 10, 20, and 50 per cent

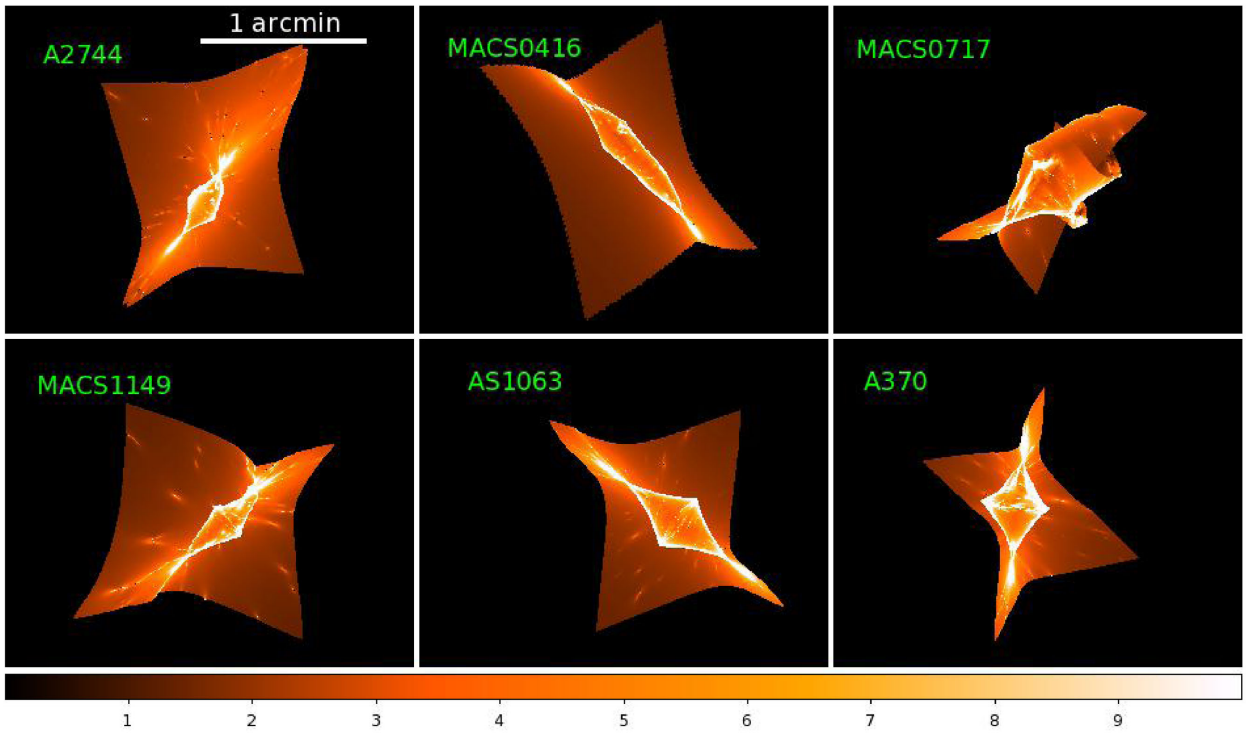

Figure 13. Source-plane magnification maps corresponding to the expected ACS+WFC3 coverage of the Frontier Field clusters. The colour scale gives the magnification value.

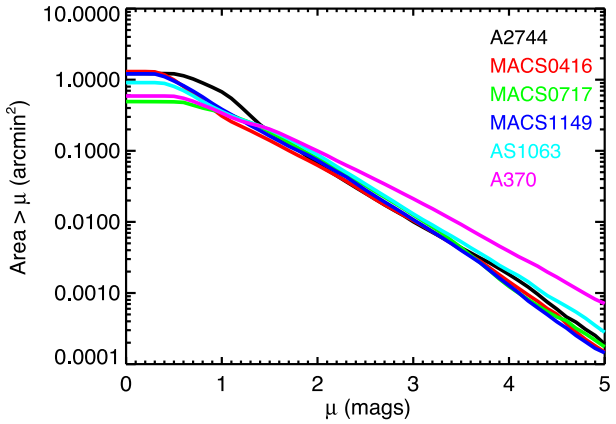

Figure 14. Surface area in the source plane covered by the ACS+WFC3 region (see Fig. 13) at a magnification above a given threshold μ.

The expected number counts at $z \sim 7$ demonstrate the advantage provided by cluster lenses compared to a blank field of the same sky coverage. The significant increase of bright sources thanks to gravitational lensing causes a *positive magnification bias* at observed AB magnitudes < 27, owing to the steep slope of the bright end of the UV luminosity function (Maizy et al. 2010). This bright-end boost in the number counts exceeds a factor of 3 at mag < 26, which is the typical limit for spectroscopic follow-up with current 8–10m class telescopes. The effect is even stronger at $z \sim 9$ and $z \sim 11$ (Fig. 15).

The above predictions have already been tested by the deep near-infrared observations of the HFF cluster A2744, performed at the end of 2013. Although ACS observations of matching depth are still lacking, the first searches for high-redshift galaxies behind this cluster have independently identified 15 dropouts at $z \sim 6-7$ down to an AB magnitude of $J = 28$ (Atek et al. 2014), and 18 dropouts at $z > 7$ down to an AB magnitude $H = 29$ (Laporte et al. 2014; Zheng et al. 2014). These numbers are slightly higher than the predictions for $z \sim 7$ and $z \sim 9$ dropouts in this cluster ($\sim$10 sources per $\Delta z = 1$), due to either contamination of these dropout samples by lower redshift sources (including low-mass stars), or most likely cosmic variance between cluster fields.

In summary, we expect a total of $\sim$200 $z = 7$ dropouts, $\sim$70 $z = 9$ dropouts and 5–10 dropouts at $z = 11$ in the six HFF, per redshift interval $\Delta z = 1$, and down to an observed AB magnitude of 29. While the number of high-redshift galaxies detected to this magnitude limit is very similar to that found in blank fields, gravitational magnification, which reaches a factor of $\sim$1–3 mag in the central regions of the HFF images, is the only way to access dropouts at even fainter magnitudes, down to m(AB) = 30–32, 2 mag fainter than the limits of the *Hubble Ultra Deep Field*. It will also increase (by a factor of at least 3) the survey sensitivity for galaxies at the highest redshifts (up to $z \sim 11$) at observed magnitudes m(AB) < 27.

We hope that the results of our efforts to calibrate the six HFF cluster lenses, described in this paper and made available to the community via the HFF website, will prove useful for the quantitative scientific exploitation of the HFF initiative and our quest to unravel the mysteries of the epoch of re-ionization.

ACKNOWLEDGEMENTS

JR acknowledges support from the ERC starting grant CALENDS and the CIG grant 294074. MJ, ML and EJ acknowledge the Mésocentre d'Aix-Marseille Université (project number: 14b030). This has also benefited from the facilities offered by CeSAM (Centre de donneS Astrophysique de Marseille).[3] ML

[3] http://lam.oamp.fr/cesam/

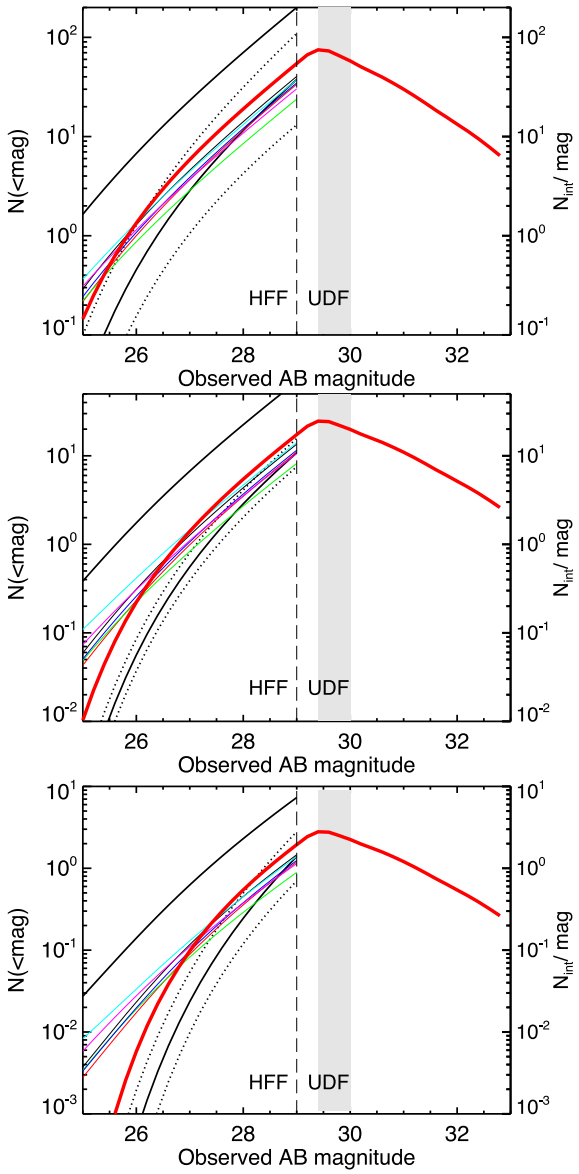

Figure 15. Predicted number of high-redshift sources at $z = 7$ (top), $z = 9$ (middle) and $z = 11$ (bottom panel), per redshift interval $\Delta z = 1$, assuming a blank field with typical errors (bottom black solid and dotted lines), each of the six FF clusters in turn (same colours as Fig. 13), and the sum over all fields (top solid black line). Overplotted as a solid-dotted line in each panel are the total intrinsic counts (per magnitude bin, corrected for magnification) expected in the FF observations. The dashed limit and the grey region mark the limiting magnitudes for HFF and the UDF, respectively.

acknowledges the Centre National de la Recherche Scientifique (CNRS) for its support. JPK and HA acknowledge support from the ERC advanced grant LIDA. This work was supported by the Leverhulme Trust (grant number PLP-2011-003) and Science and Technology Facilities Council (grant number ST/F001166/1). PN gratefully acknowledges support from the NSF via grant the AST-1009444.

REFERENCES

Abell G. O., 1958, ApJS, 3, 211
Abell G. O., Corwin H. G., Jr, Olowin R. P., 1989, ApJS, 70, 1
Atek H. et al., 2014, ApJ, 786, 60
Bartelmann M., 2001, in Brainerd T. G., Kochanek C. S., eds, ASP Conf. Ser. Vol. 237, Gravitational Lensing: Recent Progress and Future Go, Astron. Soc. Pac., San Francisco, p. 421
Bertin E., Arnouts S., 1996, A&AS, 117, 393
Boone F. et al., 2013, A&A, 559, L1
Bouwens R. J. et al., 2009, ApJ, 690, 1764
Bouwens R. J. et al., 2011, ApJ, 737, 90
Bouwens R. J. et al., 2014, ApJ, preprint (arXiv:1403.4295)
Bradač M. et al., 2006, ApJ, 652, 937
Bradač M. et al., 2009, ApJ, 706, 1201
Broadhurst T. et al., 2005, ApJ, 621, 53
Casertano S. et al., 2000, AJ, 120, 2747
Christensen L. et al., 2012, MNRAS, 427, 1953
Coe D. et al., 2013, ApJ, 762, 32
Ebeling H., Edge A. C., Henry J. P., 2001, ApJ, 553, 668
Ebeling H., Barrett E., Donovan D., Ma C.-J., Edge A. C., van Speybroeck L., 2007, ApJ, 661, L33
Ebeling H., Ma C. J., Kneib J.-P., Jullo E., Courtney N. J. D., Barrett E., Edge A. C., Le Borgne J.-F., 2009, MNRAS, 395, 1213
Ebeling H., Ma C.-J., Barrett E., 2014, ApJS, 211, 21
Egami E. et al., 2010, A&A, 518, L12
Ellis R., Santos M. R., Kneib J.-P., Kuijken K., 2001, ApJ, 560, L119
Grillo C. et al., 2014, ApJ, preprint (arXiv:1407.7866)
Jauzac M. et al., 2012, MNRAS, 426, 3369 (J12)
Jullo E., Kneib J.-P., 2009, MNRAS, 395, 1319
Jullo E., Kneib J.-P., Limousin M., Elíasdóttir Á., Marshall P. J., Verdugo T., 2007, New. J. Phys., 9, 447
Jullo E., Natarajan P., Kneib J.-P., D'Aloisio A., Limousin M., Richard J., Schimd C., 2010, Science, 329, 924
Kneib J.-P., Natarajan P., 2011, A&AR, 19, 47
Kneib J.-P., Ellis R. S., Smail I., Couch W. J., Sharples R. M., 1996, ApJ, 471, 643
Kneib J.-P., Ellis R. S., Santos M. R., Richard J., 2004, ApJ, 607, 697
Laporte N. et al., 2014, A&A, 562, L8
Leauthaud A. et al., 2007, ApJS, 172, 219 (L07)
Limousin M. et al., 2007, ApJ, 668, 643
Limousin M. et al., 2012, A&A, 544, A71
Livermore R. C. et al., 2012, MNRAS, 427, 688
Maizy A., Richard J., de Leo M. A., Pelló R., Kneib J. P., 2010, A&A, 509, A105
Mann A. W., Ebeling H., 2012, MNRAS, 420, 2120
Medezinski E. et al., 2014, ApJ, 777, 43
Merten J. et al., 2011, MNRAS, 417, 333
Monna A. et al., 2014, MNRAS, 438, 1417
Natarajan P., Kneib J.-P., 1997, MNRAS, 287, 833
Natarajan P., De Lucia G., Springel V., 2007, MNRAS, 376, 180
Owers M. S., Randall S. W., Nulsen P. E. J., Couch W. J., David L. P., Kempner J. C., 2011, ApJ, 728, 27
Postman M. et al., 2012, ApJS, 199, 25
Rhodes J., Refregier A., Groth E. J., 2000, ApJ, 536, 79
Richard J., Stark D. P., Ellis R. S., George M. R., Egami E., Kneib J.-P., Smith G. P., 2008, ApJ, 685, 705
Richard J., Pei L., Limousin M., Jullo E., Kneib J. P., 2009, A&A, 498, 37
Richard J., Kneib J.-P., Limousin M., Edge A., Jullo E., 2010a, MNRAS, 402, L44
Richard J. et al., 2010b, MNRAS, 404, 325
Richard J., Jones T., Ellis R., Stark D. P., Livermore R., Swinbank M., 2011, MNRAS, 413, 643
Rix H.-W. et al., 2004, ApJS, 152, 163
Schechter P., 1976, ApJ, 203, 297
Schmidt K. B. et al., 2014, ApJ, 782, L36
Smail I., Dickinson M., 1995, ApJ, 455, L99
Smail I. et al., 2007, ApJ, 654, L33
Smith G. P., Kneib J.-P., Smail I., Mazzotta P., Ebeling H., Czoske O., 2005, MNRAS, 359, 417
Smith G. P. et al., 2009, ApJ, 707, L163
Soucail G., Mellier Y., Fort B., Mathez G., Cailloux M., 1988, A&A, 191, L19

Soucail G., Kneib J.-P., Golse G., 2004, A&A, 417, L33
Swinbank A. M. et al., 2009, MNRAS, 400, 1121
Vanzella E. et al., 2014, ApJ, 783, L12
Wong K. C., Ammons S. M., Keeton C. R., Zabludoff A. I., 2012, ApJ, 752, 104
Zheng W. et al., 2014, preprint (arXiv:1402.6743)
Zitrin A., Broadhurst T., Barkana R., Rephaeli Y., Benítez N., 2011, MNRAS, 410, 1939
Zitrin A. et al., 2012, ApJ, 749, 97
Zitrin A. et al., 2013, ApJ, 762, L30

APPENDIX A: ARCHIVAL *HST* OBSERVATIONS OF THE HFF

Table A1. Archival *HST* imaging observations (ACS and WFC3) broad-band filters only of the HFF as of 2013 July. The fields are listed in the planned order of observation.

Target	R.A. (J2000)	Dec.	Instrument	Filter	t_{obs}	Data set	Obs. date
A2744-South	00 14 18.7	−30 23 34	ACS	*F435W*	2725	JB5G08010	2009-10-30
A2744-South	00 14 18.6	−30 23 37	ACS	*F435W*	5356	JB5G06010	2009-10-30
A2744-South	00 14 18.6	−30 23 37	ACS	*F606W*	5356	JB5G04010	2009-10-29
A2744-South	00 14 18.7	−30 23 34	ACS	*F606W*	1269	JB5G08YYQ	2009-10-30
A2744-South	00 14 18.6	−30 23 37	ACS	*F814W*	5356	JB5G02010	2009-10-27
A2744-South	00 14 18.7	−30 23 34	ACS	*F814W*	1268	JB5G08YXQ	2009-10-30
A2744-North	00 14 22.2	−30 22 33	ACS	*F435W*	2725	JB5G07010	2009-10-30
A2744-North	00 14 22.1	−30 22 36	ACS	*F435W*	5356	JB5G05010	2009-10-29
A2744-North	00 14 22.1	−30 22 36	ACS	*F606W*	5356	JB5G03010	2009-10-27
A2744-North	00 14 22.2	−30 22 33	ACS	*F606W*	1269	JB5G07YQQ	2009-10-30
A2744-North	00 14 22.2	−30 22 33	ACS	*F814W*	1268	JB5G07YPQ	2009-10-30
A2744-North	00 14 22.1	−30 22 36	ACS	*F814W*	5356	JB5G01010	2009-10-27
MACSJ0416−2403	04 16 08.4	−24 04 21	WFC3	*F225W*	3634	IBSTA6030	2012-08-18
MACSJ0416−2403	04 16 08.4	−24 04 21	WFC3	*F275W*	3684	IBSTB3040	2012-09-02
MACSJ0416−2403	04 16 08.4	−24 04 21	WFC3	*F336W*	2360	IBSTB6030	2012-09-14
MACSJ0416−2403	04 16 08.4	−24 04 21	WFC3	*F390W*	1156	IBSTB3030	2012-09-02
MACSJ0416−2403	04 16 08.4	−24 04 21	WFC3	*F390W*	1251	IBSTA6040	2012-08-18
MACSJ0416−2403	04 16 08.4	−24 04 20	ACS	*F435W*	1020	JBSTB5020	2012-09-14
MACSJ0416−2403	04 16 08.4	−24 04 21	ACS	*F435W*	1032	JBSTB0010	2012-08-20
MACSJ0416−2403	04 16 08.4	−24 04 21	ACS	*F475W*	1032	JBSTA1010	2012-07-24
MACSJ0416−2403	04 16 08.4	−24 04 21	ACS	*F475W*	1032	JBSTB7010	2012-09-27
MACSJ0416−2403	04 16 08.4	−24 04 20	ACS	*F606W*	986	JBSTA8020	2012-08-31
MACSJ0416−2403	04 16 08.4	−24 04 21	ACS	*F606W*	1032	JBSTA3010	2012-08-05
MACSJ0416−2403	04 16 08.4	−24 04 21	ACS	*F625W*	985	JBSTB0020	2012-08-20
MACSJ0416−2403	04 16 08.4	−24 04 21	ACS	*F625W*	1032	JBSTA0010	2012-07-24
MACSJ0416−2403	04 16 08.4	−24 04 20	ACS	*F775W*	1016	JBSTB2020	2012-09-02
MACSJ0416−2403	04 16 08.4	−24 04 21	ACS	*F775W*	1015	JBSTA1020	2012-07-24
MACSJ0416−2403	04 16 08.4	−24 04 20	ACS	*F814W*	986	JBSTA3020	2012-08-05
MACSJ0416−2403	04 16 08.4	−24 04 20	ACS	*F814W*	987	JBSTA5020	2012-08-18
MACSJ0416−2403	04 16 08.4	−24 04 21	ACS	*F814W*	1032	JBSTA8010	2012-08-31
MACSJ0416−2403	04 16 08.4	−24 04 21	ACS	*F814W*	1032	JBSTB5010	2012-09-14
MACSJ0416−2403	04 16 08.4	−24 04 21	ACS	*F850LP*	1019	JBSTA0020	2012-07-24
MACSJ0416−2403	04 16 08.4	−24 04 20	ACS	*F850LP*	1003	JBSTB7020	2012-09-27
MACSJ0416−2403	04 16 08.4	−24 04 21	ACS	*F850LP*	1032	JBSTA5010	2012-08-18
MACSJ0416−2403	04 16 08.4	−24 04 21	ACS	*F850LP*	1032	JBSTB2010	2012-09-02
MACSJ0416−2403	04 16 08.4	−24 04 20	WFC3	*F105W*	1305	IBSTB6050	2012-09-14
MACSJ0416−2403	04 16 08.4	−24 04 21	WFC3	*F105W*	1509	IBSTA4020	2012-08-05
MACSJ0416−2403	04 16 08.4	−24 04 21	WFC3	*F110W*	1509	IBSTA2020	2012-07-24
MACSJ0416−2403	04 16 08.4	−24 04 21	WFC3	*F110W*	1006	IBSTA9030	2012-08-31
MACSJ0416−2403	04 16 08.4	−24 04 21	WFC3	*F125W*	1509	IBSTB1020	2012-08-20
MACSJ0416−2403	04 16 08.4	−24 04 21	WFC3	*F125W*	1006	IBSTB8030	2012-09-27
MACSJ0416−2403	04 16 08.4	−24 04 20	WFC3	*F140W*	1005	IBSTB1030	2012-08-20
MACSJ0416−2403	04 16 08.4	−24 04 21	WFC3	*F140W*	1306	IBSTB6040	2012-09-14
MACSJ0416−2403	04 16 08.4	−24 04 20	WFC3	*F160W*	1005	IBSTA2030	2012-07-24
MACSJ0416−2403	04 16 08.4	−24 04 21	WFC3	*F160W*	1509	IBSTA9020	2012-08-31
MACSJ0416−2403	04 16 08.4	−24 04 21	WFC3	*F160W*	1509	IBSTB8020	2012-09-27
MACSJ0416−2403	04 16 08.4	−24 04 21	WFC3	*F160W*	1006	IBSTA4030	2012-08-05
MACS0717+3745	07 17 32.6	+37 45 00	WFC3	*F225W*	3645	BFLA6030	2011-11-19
MACS0717+3745	07 17 32.6	+37 45 00	WFC3	*F275W*	3723	BFLB3040	2011-09-20
MACS0717+3745	07 17 32.6	+37 45 00	WFC3	*F336W*	2391	BFLB6030	2011-10-10
MACS0717+3745	07 17 32.6	+37 45 00	WFC3	*F390W*	1254	BFLA6040	2011-11-19
MACS0717+3745	07 17 32.6	+37 45 00	WFC3	*F390W*	1179	BFLB3030	2011-09-20
MACS0717+3745	07 17 32.6	+37 45 00	ACS	*F435W*	1032	JBFLA3010	2011-10-29

Table A1 – *continued*

Target	R.A. (J2000)	Dec.	Instrument	Filter	t_{obs}	Data set	Obs. date
MACS0717+3745	07 17 32.7	+37 45 01	ACS	*F435W*	994	JBFLB5020	2011-10-10
MACS0717+3745	07 17 32.7	+37 45 01	ACS	*F475W*	1000	JBFLA3020	2011-10-29
MACS0717+3745	07 17 32.6	+37 45 00	ACS	*F475W*	1032	JBFLB7010	2011-10-30
MACSJ0717+3745	07 17 32.9	+37 45 05	ACS	*F555W*	4470	J8QU05010	2004-04-02
MACSJ0717.5+3745-POS5	07 17 32.0	+37 44 48	ACS	*F606W*	1980	J97001010	2005-01-25
MACSJ0717.5+3745-POS5	07 17 43.4	+37 47 01	ACS	*F606W*	1980	J97005010	2005-01-30
MACS0717+3745	07 17 32.6	+37 45 00	ACS	*F625W*	1032	JBFLA0010	2011-10-10
MACS0717+3745	07 17 32.6	+37 45 00	ACS	*F625W*	1032	JBFLB5010	2011-10-10
MACS0717+3745	07 17 32.7	+37 45 01	ACS	*F775W*	1023	JBFLA8020	2011-12-08
MACS0717+3745	07 17 32.6	+37 45 00	ACS	*F775W*	1023	JBFLB0020	2011-08-31
MACSJ0717+3745	07 17 32.9	+37 45 05	ACS	*F814W*	2097	J9OI04010	2006-10-13
MACSJ0717+3745	07 17 32.9	+37 45 05	ACS	*F814W*	4560	J8QU05020	2004-04-02
MACSJ0717.5+3745-POS5	07 17 43.4	+37 47 01	ACS	*F814W*	4020	J97005020	2005-01-30
MACSJ0717+3745	07 17 32.9	+37 45 05	ACS	*F814W*	2236	J9DD04010	2005-10-25
MACS0717+3745	07 17 32.6	+37 45 00	ACS	*F850LP*	1026	JBFLA0020	2011-10-10
MACS0717+3745	07 17 32.6	+37 45 00	ACS	*F850LP*	1032	JBFLA8010	2011-12-08
MACS0717+3745	07 17 32.6	+37 45 00	ACS	*F850LP*	1032	JBFLB0010	2011-08-31
MACS0717+3745	07 17 32.7	+37 45 01	ACS	*F850LP*	1010	JBFLB7020	2011-10-30
MACS0717+3745	07 17 32.6	+37 45 00	WFC3	*F105W*	1509	IBFLA4020	2011-10-29
MACS0717+3745	07 17 32.7	+37 45 00	WFC3	*F105W*	1306	IBFLB6050	2011-10-11
MACS0717+3745	07 17 32.6	+37 45 00	WFC3	*F110W*	1509	IBFLA2020	2011-10-10
MACS0717+3745	07 17 32.6	+37 44 59	WFC3	*F110W*	1006	IBFLA9030	2011-12-09
MACS0717+3745	07 17 32.6	+37 45 00	WFC3	*F125W*	1509	IBFLB1020	2011-08-31
MACS0717+3745	07 17 32.6	+37 44 59	WFC3	*F125W*	1006	IBFLB8030	2011-10-30
MACS0717+3745	07 17 32.6	+37 44 59	WFC3	*F140W*	1006	IBFLA4030	2011-10-29
MACS0717+3745	07 17 32.6	+37 45 00	WFC3	*F140W*	1306	IBFLB6040	2011-10-11
MACS0717+3745	07 17 32.6	+37 45 00	WFC3	*F160W*	1006	IBFLA2030	2011-10-10
MACS0717+3745	07 17 32.6	+37 45 00	WFC3	*F160W*	1509	IBFLA9020	2011-12-09
MACS0717+3745	07 17 32.6	+37 45 00	WFC3	*F160W*	1006	IBFLB1030	2011-09-01
MACS0717+3745	07 17 32.6	+37 45 00	WFC3	*F160W*	1509	IBFLB8020	2011-10-30
MACS1149+2223	11 49 35.7	+22 23 55	WFC3	*F225W*	1194	IBF5A6020	2011-02-13
MACS1149+2223	11 49 35.7	+22 23 55	WFC3	*F225W*	2362	IBF5B6030	2011-02-27
MACS1149+2223	11 49 35.7	+22 23 55	WFC3	*F275W*	1194	IBF5A6030	2011-02-13
MACS1149+2223	11 49 35.7	+22 23 55	WFC3	*F275W*	2414	IBF5B4020	2011-02-15
MACS1149+2223	11 49 35.7	+22 23 55	WFC3	*F336W*	1195	IBF5A7020	2011-02-13
MACS1149+2223	11 49 35.7	+22 23 54	WFC3	*F336W*	1196	IBF5B3030	2011-02-15
MACS1149+2223	11 49 35.7	+22 23 55	WFC3	*F390W*	1196	IBF5A7030	2011-02-13
MACS1149+2223	11 49 35.7	+22 23 55	WFC3	*F390W*	1195	IBF5B3020	2011-02-15
MACS1149+2223	11 49 35.7	+22 23 55	ACS	*F435W*	1032	JBF5A5010	2011-02-13
MACS1149+2223	11 49 35.7	+22 23 56	ACS	*F435W*	956	JBF5B5020	2011-02-27
MACS1149+2223	11 49 35.7	+22 23 56	ACS	*F475W*	1034	JBF5A3020	2011-01-30
MACS1149+2223	11 49 35.7	+22 23 55	ACS	*F475W*	1034	JBF5B0020	2010-12-04
MACSJ1149+2223	11 49 35.5	+22 24 04	ACS	*F555W*	4500	J8QU08010	2004-04-22
MACS1149+2223	11 49 35.7	+22 23 55	ACS	*F606W*	1032	JBF5A0010	2011-01-15
MACS1149+2223	11 49 35.7	+22 23 55	ACS	*F606W*	1032	JBF5B5010	2011-02-27
MACS1149+2223	11 49 35.7	+22 23 56	ACS	*F625W*	1015	JBF5A5020	2011-02-13
MACS1149+2223	11 49 35.7	+22 23 55	ACS	*F625W*	1032	JBF5B7010	2011-03-09
MACS1149+2223	11 49 35.7	+22 23 56	ACS	*F775W*	994	JBF5A8020	2011-02-27
MACS1149+2223	11 49 35.7	+22 23 56	ACS	*F775W*	1053	JBF5B7020	2011-03-09
MACSJ1149+2223	11 49 35.5	+22 24 04	ACS	*F814W*	4590	J8QU08020	2004-04-22
MACSJ1149+2223	11 49 35.5	+22 24 04	ACS	*F814W*	2184	J9DD07010	2006-05-25
MACS1149+2223	11 49 35.7	+22 23 55	ACS	*F850LP*	1044	JBF5A0020	2011-01-15
MACS1149+2223	11 49 35.7	+22 23 55	ACS	*F850LP*	1032	JBF5A3010	2011-01-30
MACS1149+2223	11 49 35.7	+22 23 55	ACS	*F850LP*	1032	JBF5A8010	2011-02-27
MACS1149+2223	11 49 35.7	+22 23 55	ACS	*F850LP*	1032	JBF5B0010	2010-12-04
MACS1149+2223	11 49 35.7	+22 23 55	WFC3	*F105W*	1509	IBF5A4020	2011-01-30
MACS1149+2223	11 49 35.7	+22 23 55	WFC3	*F105W*	1306	IBF5B6050	2011-02-27
MACS1149+2223	11 49 35.7	+22 23 55	WFC3	*F110W*	1509	IBF5A2020	2011-01-16
MACS1149+2223	11 49 35.7	+22 23 54	WFC3	*F110W*	906	IBF5A9030	2011-02-27
MACS1149+2223	11 49 35.7	+22 23 55	WFC3	*F125W*	1509	IBF5B1020	2010-12-04
MACS1149+2223	11 49 35.7	+22 23 54	WFC3	*F125W*	1006	IBF5B8030	2011-03-09
MACS1149+2223	11 49 35.7	+22 23 54	WFC3	*F140W*	1006	IBF5A4030	2011-01-30
MACS1149+2223	11 49 35.7	+22 23 55	WFC3	*F140W*	1306	IBF5B6040	2011-02-27

Table A1 – *continued*

Target	R.A. (J2000)	Dec.	Instrument	Filter	t_{obs}	Data set	Obs. date
MACS1149+2223	11 49 35.7	+22 23 55	WFC3	*F160W*	1006	IBF5A2030	2011-01-16
MACS1149+2223	11 49 35.7	+22 23 55	WFC3	*F160W*	1509	IBF5A9020	2011-02-27
MACS1149+2223	11 49 35.7	+22 23 55	WFC3	*F160W*	1005	IBF5B1030	2010-12-04
MACS1149+2223	11 49 35.7	+22 23 55	WFC3	*F160W*	1509	IBF5B8020	2011-03-09
RXJ2248−4431	22 48 44.0	−44 31 51	WFC3	*F225W*	3574	BSUA6030	2012-09-24
RXJ2248−4431	22 48 44.0	−44 31 51	WFC3	*F275W*	3637	BSUB3040	2012-10-09
RXJ2248−4431	22 48 44.0	−44 31 51	WFC3	*F336W*	2359	BSUB6030	2012-10-22
RXJ2248−4431	22 48 44.0	−44 31 51	WFC3	*F390W*	1215	BSUA6040	2012-09-24
RXJ2248−4431	22 48 44.0	−44 31 51	WFC3	*F390W*	1155	BSUB3030	2012-10-09
RXJ2248−4431	22 48 44.0	−44 31 51	ACS	*F435W*	1032	JBSUA8010	2012-10-04
RXJ2248−4431	22 48 44.0	−44 31 52	ACS	*F435W*	1019	JBSUB5020	2012-10-22
RXJ2248−4431	22 48 44.0	−44 31 51	ACS	*F475W*	1032	JBSUA1010	2012-08-30
RXJ2248−4431	22 48 44.0	−44 31 51	ACS	*F475W*	1032	JBSUB7010	2012-11-04
RXJ2248−4431	22 48 44.0	−44 31 52	ACS	*F606W*	985	JBSUA3020	2012-09-12
RXJ2248−4431	22 48 44.0	−44 31 51	ACS	*F606W*	1003	JBSUB0020	2012-09-26
RXJ2248−4431	22 48 44.0	−44 31 51	ACS	*F625W*	1032	JBSUA0010	2012-08-30
RXJ2248−4431	22 48 44.0	−44 31 51	ACS	*F625W*	1032	JBSUB0010	2012-09-26
RXJ2248−4431	22 48 44.0	−44 31 51	ACS	*F775W*	1014	JBSUA1020	2012-08-30
RXJ2248−4431	22 48 44.0	−44 31 52	ACS	*F775W*	1015	JBSUB2020	2012-10-09
RXJ2248−4431	22 48 44.0	−44 31 51	ACS	*F814W*	1032	JBSUA3010	2012-09-12
RXJ2248−4431	22 48 44.0	−44 31 52	ACS	*F814W*	986	JBSUA5020	2012-09-24
RXJ2248−4431	22 48 44.0	−44 31 52	ACS	*F814W*	1018	JBSUA8020	2012-10-04
RXJ2248−4431	22 48 44.0	−44 31 51	ACS	*F814W*	1032	JBSUB5010	2012-10-22
ANY	22 48 44.7	−44 31 38	ACS	*F814W*	1918	JC6HS1010	2012-11-19
RXJ2248−4431	22 48 44.0	−44 31 51	ACS	*F850LP*	1018	JBSUA0020	2012-08-30
RXJ2248−4431	22 48 44.0	−44 31 51	ACS	*F850LP*	1032	JBSUA5010	2012-09-24
RXJ2248−4431	22 48 44.0	−44 31 51	ACS	*F850LP*	1032	JBSUB2010	2012-10-09
RXJ2248−4431	22 48 44.0	−44 31 52	ACS	*F850LP*	1002	JBSUB7020	2012-11-04
RXJ2248−4431	22 48 44.0	−44 31 51	WFC3	*F105W*	1509	IBSUA4020	2012-09-12
RXJ2248−4431	22 48 43.9	−44 31 52	WFC3	*F105W*	1306	IBSUB6050	2012-10-22
RXJ2248−4431	22 48 44.0	−44 31 51	WFC3	*F110W*	1509	IBSUA2020	2012-08-30
RXJ2248−4431	22 48 43.9	−44 31 51	WFC3	*F110W*	1006	IBSUA9030	2012-10-04
RXJ2248−4431	22 48 44.0	−44 31 51	WFC3	*F125W*	1509	IBSUB1020	2012-09-26
RXJ2248−4431	22 48 43.9	−44 31 51	WFC3	*F125W*	1006	IBSUB8030	2012-11-04
RXJ2248−4431	22 48 43.9	−44 31 51	WFC3	*F140W*	1006	IBSUA4030	2012-09-12
RXJ2248−4431	22 48 44.0	−44 31 51	WFC3	*F140W*	1306	IBSUB6040	2012-10-22
RXJ2248−4431	22 48 44.0	−44 31 51	WFC3	*F160W*	1006	IBSUA2030	2012-08-30
RXJ2248−4431	22 48 44.0	−44 31 51	WFC3	*F160W*	1509	IBSUA9020	2012-10-04
RXJ2248−4431	22 48 44.0	−44 31 52	WFC3	*F160W*	1006	IBSUB1030	2012-09-26
RXJ2248−4431	22 48 44.0	−44 31 51	WFC3	*F160W*	1509	IBSUB8020	2012-11-04
ABELL-0370	02 39 51.0	−01 34 50	ACS	*F475W*	6780	JABU01030	2009-07-16
SMMJ02399−0136	02 39 52.0	−01 35 58	ACS	*F475W*	2250	JB3402011	2010-12-25
ABELL-0370	02 39 51.0	−01 34 50	ACS	*F625W*	2040	JABU01010	2009-07-16
ABELL-0370	02 39 51.0	−01 34 50	ACS	*F814W*	3840	JABU01020	2009-07-16
ABELL-370	02 39 51.5	−01 34 46	ACS	*F814W*	4720	JB5M22010	2010-12-20
ABELL-370	02 39 51.5	−01 34 48	ACS	*F814W*	4880	JB5M22020	2010-12-20
ABELL-370-WFC3	02 39 53.9	−01 34 32	WFC3	*F110W*	2612	IB5M12020	2010-12-19
ABELL-370-WFC3	02 39 53.9	−01 34 32	WFC3	*F160W*	2412	IB5M12010	2010-12-19

This paper has been typeset from a TEX/LATEX file prepared by the author.